Investigation of a U-Shaped Fuel Cell Flow Channel with Particle Image Velocimetry (PIV)

by

Jonathan Jackie Martin
B.S.E., Loyola Marymount University, 2002

A Thesis Submitted in Partial Fulfillment of the requirements for the degree of

Master of Applied Science

in the Department of Mechanical Engineering

We accept this thesis as conforming to the required standard

_____
Dr. N. Djilali, Co-Supervisor (Department of Mechanical Engineering)

_____
Dr. P. Oshkai, Co-Supervisor (Department of Mechanical Engineering)

_____
Dr. P. Wild, Member (Department of Mechanical Engineering)

_____
Dr. Rolf Lueck, External Examiner (School of Earth and Ocean Sciences)

© Jonathan Jackie Martin, 2004
University of Victoria

ABSTRACT

Flow through an experimental model of a U-shaped flow channel is used to investigate the hydrodynamic phenomena that occur within serpentine reactant transport channels of fuel cells. Achieving effective mixing within these channels is crucial for the proper operation of the fuel cell and proper understanding and characterization of the underlying fluid dynamics is required. Particle image velocimetry (PIV) is used to investigate the three-dimensional structure of the flow by analyzing the velocity and associated vorticity field over two perpendicular channel cross-sections. A range of Reynolds numbers, 109 ? Re ? 872, corresponding to flow rates encountered in a fuel cell operating at low to medium current densities is investigated. The effect of the flow rate is characterized in terms of the instantaneous and time-averaged representations of the velocity vectors, out-of-plane vorticity and the velocity streamlines.

At the lowest Reynolds numbers, the flow is steady and is characterized by high vorticity regions associated with shear layers separating from the sharp convex corners of the U-bend and reattaching on downstream surfaces. The flow also exhibits the classical secondary Dean flow pattern with two symmetric circulation zones. Transition takes place in the range 381 ? Re ? 436 as the two recirculation zones, which originally develop in the U-bend region, merge into one separation region. This transition is accompanied by the generation of additional vortices in the secondary flow plane. The relationship between the flow in both planes and the transition is examined along with properties of the instability including RMS, Reynolds stress, and the oscillation frequency. The quantitative flow visualization results obtained presented here should be

useful in guiding numerical models of fuel cells, and indicate that the commonly used assumption of steady laminar flow should be revisited, and alternative models developed.

Examiners:

_____

Dr. N. Djilali, Co-Supervisor (Department of Mechanical Engineering)

_____

Dr. P. Oshkai, Co-Supervisor (Department of Mechanical Engineering)

_____

Dr. P. Wild, Member (Department of Mechanical Engineering)

_____

Dr. Rolf Lueck, External Examiner (School of Earth and Ocean Sciences)

TABLE OF CONTENTS

List of Figures

Nomenclature

Symbol	Description	Units
$\langle u' v' \rangle$	primary Reynolds stress	$m^2 \cdot s^{-2}$
$\langle u' w' \rangle$	secondary Reynolds stress	$m^2 \cdot s^{-2}$
a	hydraulic diameter	mm
C	correlation strength	—
f	oscillation frequency of the flow	Hz
I	image intensity	—
Q	peak ratio	—
R	radius of curvature	mm
Rc	curvature ratio	—
Re	Reynolds number	—
U	average velocity	$m \cdot s^{-1}$
U_b	bulk velocity based on flowrate	$m \cdot s^{-1}$
U_o	velocity in the oscillating shear layer	$m \cdot s^{-1}$
U_p	velocity in the primary plane	$m \cdot s^{-1}$
U_s	velocity in the secondary plane	$m \cdot s^{-1}$
u	x-component of velocity	$m \cdot s^{-1}$
u'	fluctuating component of u	$m \cdot s^{-1}$
v	y-component of velocity	$m \cdot s^{-1}$
v'	fluctuating component of v	$m \cdot s^{-1}$
$|\underline{V}|_{rms}$	root-mean square velocity fluctuations	$m \cdot s^{-1}$
w	z-component of velocity	$m \cdot s^{-1}$

w´			fluctuating component of w	$m \cdot s^{-1}$
?			wavelength of the flow oscillation	m
??	?	?	kinematic viscosity	$m^2 \cdot s^{-1}$
$?_z$			primary out-of-plane vorticity	s^{-1}
$?_y$			secondary out-of-plane vorticity	s^{-1}

ACKNOWLEDGEMENTS

Firstly, I would like to thank my supervisors Dr. Ned Djilali and Dr. Peter Oshkai for their boundless support and guidance during the many stages of this project. Their flexibility and perseverance allowed me to overcome every obstacle along the way.

For helping to keep everything in my project and education organized and running smoothly I would like to thank Susan Walton. She is an invaluable asset to all of the students, faculty and staff of IESVic.

I am grateful of Matthew Guenther and his vast computer knowledge. Without him I may never have been able to get my Matlab algorithms to run correctly. I am also grateful of all of the graduate students who helped me focus on the important things (inside and outside of the laboratory).

To my family, who has always been there for me, especially in times when I have questioned my abilities. I want to thank you from the bottom of my heart for helping me become the man I am today.

CHAPTER 1   INTRODUCTION

1.1   Background and Motivation

In a Proton Exchange Membrane (PEM) fuel cell, the membrane electrode assembly (MEA), where the electrochemical reaction and transport processes take place, is typically sandwiched between two bipolar plates, which serve to (a) collect the electric current, and (b) supply the reactants through the embedded flow channels. The operation of a PEMFC depends critically on the effective distribution of air and hydrogen in these flow channels, and on the maintenance of both operating temperature and of well humidified conditions in the membrane. The distribution of reactant gases is particularly critical on the cathode (oxygen) side, which is prone to mass transport limitations. The cathode is usually fed with air at relatively low pressure (1~3 atmospheres). As the electrochemical reaction proceeds, the concentration of oxygen in the airflow channels gradually drops. Because of imperfect mixing, the concentration drop is largest in the vicinity of the electrodes. At high current densities, the rate at which oxygen is supplied from the cathode side to the reaction site (catalyst layer) becomes insufficient and the cell is "starved". This so-called concentration polarization results in a significant drop in the voltage produced by the cell, thus limiting the power output. Effective mixing in the reactant gas flow channels is therefore highly desirable.

The most common channel design on a bipolar plate is a serpentine design, as shown in Figure 1.1. Characterization of the fluid dynamics in the serpentine gas flow channels is essential to understanding and improving mixing. So far, the highly reactive environment of a fuel cell has been a major challenge to detailed *in-situ* measurements

during operation, and though significant progress has been made in computational modeling, the complexity of the phenomena has required a number of simplifying assumptions, and in particular the flow in these models is assumed steady and laminar (e.g. Nguyen *et al.* [1]; Siegel *et al.* [2]; Kumar and Reddy [3]; Wang *et al.* [4]).
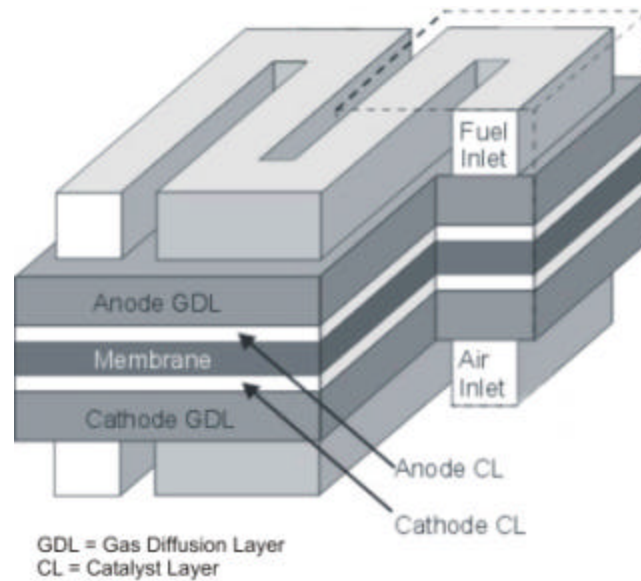
Figure 1.1: Schematic of a typical fuel cell, including a serpentine channel design.

1.2 Dean Type Flow

1.2.1 Flow In Curved Pipes

Flow in curved pipes and serpentine flow channels are encountered in a number of other engineering systems, particularly in chemical processing and heat exchangers, and such flows have been the subject of numerous experimental and numerical studies. The analytic foundations for secondary flows in curved pipes were laid by Dean [5] who established that the onset of secondary vortices in curved pipes is characterized by the ratio of the Reynolds number to the square of the product of the inertia and centrifugal forces. The non-dimensionalized parameter, referred to as the Dean number, is:

$$Dn = Re/(Rc)^{1/2} \tag{1}$$

Where the Reynolds number, Re=Ua/?, and the curvature ratio, Rc=R/a. U is the bulk mean velocity, a is the hydraulic diameter, ? is the kinematic viscosity and R is the radius of curvature.

The secondary (Dean) flow in a curved pipe, illustrated in Figure 1.2, occurs along the centerline of the tube cross-section, from the inner radius towards the outer, before recirculating back along the pipe walls and is attributed to the effect of the centrifugal pressure gradient in the main flow acting on the relatively low momentum fluid in the wall boundary layer. Although Hawthorne [6] showed that the secondary flow could occur in a perfectly inviscid flow as a result of a non-uniform distribution of velocity at the entrance, most work focuses on the centrifugal effects. Some of the more notable experimental investigations into curved pipe flow include Agrawal *et al.* [7] and Olsen and Snyder [8], while Lin and Tarbell [9] also include a numerical study. Agrawal *et al.* confirmed the existence of vortex behavior in a laser anemometer study of two semi-circular pipes, covering a Dean number range from 138 to 679. Olsen and Snyder also conducted a laser anemometer study with a similar Dean number range (100 to 500). The curvature ratios in their study were significantly smaller, however, and they noticed a damping of the secondary flow downstream of the bend similar to that predicted by Hawthorne. Lin and Tarbell investigated the effect of periodic flow, which can induce a four-vortex structure at high frequencies. One of the most comprehensive reviews of the numerical and experimental work done in curved pipes is Berger and Talbot [10].
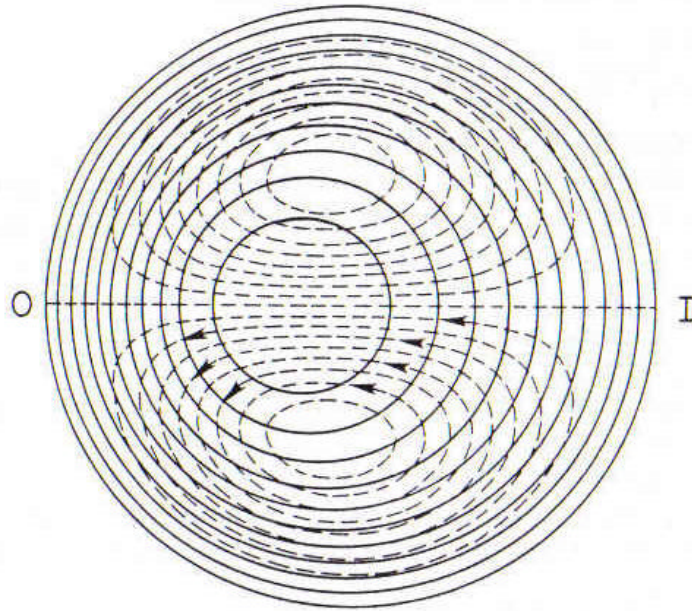
Figure 1.2: Typical Dean type flow found in curved pipes: I refers to the inner edge and O refers to the outer. [10]

1.2.2   Flow in Curved Channels of Rectangular Cross-section

While the original focus of research in curved channel flows was circular pipes, square and rectangular channels have subsequently received significant attention. Flow in square ducts differs from circular pipe flow by the onset of additional vortex structures. Since the most common application of curved square and rectangular ducts is in heat exchangers, particularly in turbines, the majority of the investigations involved turbulent flow, and in many cases rotation. Studies of laminar secondary motion in non-rotating curved channels include the experimental and numerical studies of Humphrey *et al.* [11] and Bara *et al.* [12]. In a continuation of the work performed by Bara *et al.*, Mees *et al.* [13] observed the onset of a six-cell secondary flow pattern above a Dean number of 350. An additional pair of vortices also appeared along the outer radius wall.

Gauthier *et al.* [14] did not investigate the secondary flow; but performed a visualization study of the bulk streamwise flow and observed the onset of instability at Re = 340. Although the cause of the instability is due to shear rather than separation, it is one of the few studies on unsteadiness in curved channels at low Reynolds numbers. The review by Berger and Talbot [10] also contains significant resources on curved channels of square and rectangular cross-sections.

1.2.3   Flow in Sharp U-Bends of Square Cross-section

In a large number of fuel cell designs, the bipolar plate contains serpentine channels that usually closely resemble a squared U-bend rather than a curved channel. In a U-bend channel with a 180-degree sharp turn, the flow is also affected by impingement, recirculation, and flow separation. The majority of previous studies related to sharp U-bends are primarily concerned with heat transfer phenomena. Although the literature is dominated by turbulent flow in rotating channels, studies on laminar flow in non-rotating channels are also available. The numerical study by Chintada *et al.* [15] contains an overview of the flow and heat transfer characteristics, but does not present any detailed analysis of the secondary flow. While Mochizuki *et al.* [16] focus on turbulent flow through smooth and rib-roughened serpentine channels, they do provide a nice visualization of the secondary flow during and after a sharp turn at Re = 500. Lastly, Choi *et al.* [17] do not examine the secondary flow and limit their numerical study to Reynolds numbers below 500. Unsteadiness due to vortex shedding at the sharp corners was a concern at higher Reynolds numbers. The limit was based on a baffle study in open channel flow since no experimental results were available for their geometry.

In the present study, the experimental technique of Particle Imaging Velocimetry (PIV) is used to provide a detailed description of the flow in a serpentine flow channel. A 180-degree sharp turn is utilized to simulate the first two passes of a serpentine channel. The flow is characterized in terms of the instantaneous and time-averaged representations of the velocity, streamline topology, and vorticity contours. These characteristics are used to examine the secondary flow at the midpoint of the turn as well as the onset of instability in laminar flow at increasing Reynolds numbers.

1.3 PIV Fundamentals

PIV is a full-field, non-intrusive flow visualization technique. Adrian [18] produced one of the first reviews on the technique, accurately assessing the current status of the various approaches and comparing their advantages as well as their drawbacks. Implementation of PIV has continued to increase as technological advances such as faster computer processors, improved algorithms and higher resolution CCD cameras have increased the accuracy of the technique, while decreasing the cost.

The general approach of PIV is to find the velocity field of the fluid flow by analyzing the displacement of seeding particles introduced into the fluid. The density of the seeding particles is a determining factor in selecting the velocimetry technique. Particle Tracking Velocimetry (PTV) and Laser Speckle Velocimetry (LSV) can be possible alternatives. PTV is a low seeding density technique in which the displacement is determined by tracking individual particles for multiple exposures. LSV is a high-density technique in which individual particles are indistinguishable. Displacement of the fluid is induced by following the "speckle pattern" produced by the overlapping particles. While the density of particles in PIV varies, in general it is low enough such

that individual particles can be distinguished; yet high enough that individual tracking of particles is computationally impractical or deemed unnecessary. In all three techniques, most implementations use a laser sheet as a light source and a digital camera as the image acquisition device. The laser sheet is pulsed with a known time delay between the pulses. Images of the particles illuminated by the laser are recorded by the camera. A correlation algorithm is then used to determine the displacement of the particles.

Generally, there are two approaches for determining the particle displacement over the time between the laser pulses. These approaches or interrogation algorithms are respectively referred to as autocorrelation and cross-correlation algorithms. While the input for an autocorrelation algorithm is a single image with multiple exposures of the tracing particles in the flow, cross-correlation algorithms require a pair of images. The image pair consists of two separate images, each containing a single exposure of the flow field. The result of the interrogation of the particle images is a map of the instantaneous velocity distribution in the flow field, referred herein as a frame. Thus only one image is required per frame when utilizing an autocorrelation algorithm, while multiple images are required per frame in the case of a cross-correlation approach. An autocorrelation method of image interrogation is advantageous due to its lower cost, potentially higher time resolution, and the ability to extract particle acceleration information. However, since each image contains multiple exposures of the same particle, a directional ambiguity exists if this issue is not addressed in the experimental procedure. While the autocorrelation approach finds its application in certain cases, there is a trend among commercial manufacturers of PIV systems to implement various versions of the cross-correlation approach. A typical implementation of the cross-correlation method involves

breaking each image of the image pair into multiple interrogation regions. A computer algorithm is used to interrogate each pair of corresponding interrogation regions between the two images to determine the displacement of the tracing particles. Thus, for each interrogation region, a single displacement is determined. In conjunction with the time delay, the displacement is used to determine the velocity. Upon interrogation of the entirety of the image pair, a full field distribution of the instantaneous velocity is obtained.

The types of error in the measured velocity vectors can be grouped into three major groups: spurious vectors, precision error and bias error. Spurious vectors are false representations of the fluid displacement, usually caused by poor image correlation. A common and effective technique for eliminating these is through filtering. If the variation between a vector and its neighbors exceeds a certain threshold, the vector in question is removed. As a result of various error sources, minimizing the precision and bias errors within the valid vectors is considerably more complicated. These major classes of errors in PIV measurements originate primarily from experimental conditions and correlation algorithm errors. There are also additional considerations that need to be addressed when flow characteristics such as vorticity are calculated from the measured velocity field. These issues are further discussed in Section 2.2.

1.4 Thesis Objectives

The first objective is to prove in concept the ability to acquire PIV data in a fuel cell flow channel, and to assess the limitations and advantages of this technique for such applications. The second objective is to acquire a detailed understanding of the flow features in a single U-bend of a serpentine channel. An understanding of the primary and

secondary flow characteristics is required, as well as relationships between the two. While the flow channel investigated contains water and is an order of magnitude larger than the air channels commonly found in fuel cells, the results remain directly relevant to and actual fuel cell because the flow is incompressible, and dynamic similarity is ensured by using experimental Reynolds number and Dean number that correspond to expected values in a practical fuel cell. Some features, such as roughness introduced by the gas diffusion layer in a fuel cell, are not accounted for in this exploratory study, but if meaningful results are obtained, such effects as well as investigation in an active fuel cell may then be justified and planned in follow up studies. In addition to gaining insight into the characteristics of flow inside fuel cell gas distribution channels, a broad objective of this work is guidance for the numerical modeling of such flow in fuel cell models that couple convective transport and electrochemistry.

CHAPTER 2   EXPERIMENTAL SYSTEM

2.1   Experimental Apparatus

The major components of the experiment were as shown in Figure 2.1. The flow system consisted of a reservoir with a pump, a supply system with a bleed, and a flow channel. Recirculation of the water eliminated the need to constantly resupply seeding particles to the system. The supply system consisted of the bleed, a flowmeter and a valve. The flowmeter was a standard variable area type with a stainless steel ball as the float. It was graduated from 5 – 40 lph (liters/hour) at 5 lph increments. The pump could provide a maximum flow rate of 200 gph (gallons/hour) at a head of 0 inches. Even though it was set at the lowest setting of 170 gph with a head of approximately 18 inches, the flow rate was significantly higher than was needed. A bleed was installed to alleviate pulsations from the pump at the lower flow rates desired. The bleed allowed a portion of the water to bypass the flowmeter and return directly to the reservoir.
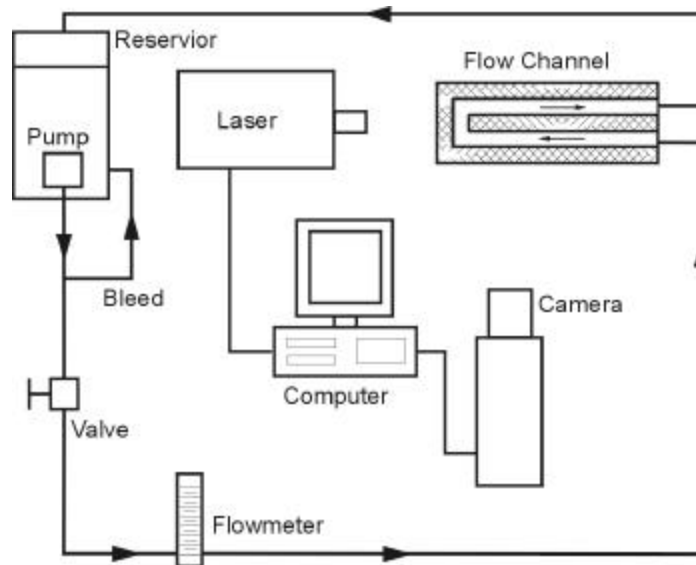
Figure 2.1: Major components of the experimental system.

The flow channel had a 12.7 mm square cross-section, with a gap of 12.7 mm between the inlet and outlet sections. The distance between the start of the square flow channel and the beginning of the U-bend was 279.4 mm. Two pieces of Plexiglas were used in the construction of the flow channel. The channel was machined into a 24 mm thick piece of Plexiglas with a seal groove around the perimeter of the channel. Surrounding the seal groove, were threads for 6-32x3/8 bolts. Bolts were used rather than glue so that the flow channel was easily accessible for cleaning, thus insuring a high level of optical clarity. The inlet and outlet of the channel were drilled and then threaded for 1/4" NPT connectors, which attached to the supply hoses. The second piece of Plexiglas was 6 mm thick and had holes drilled for the bolts. While the o-ring eliminated leaking from around the edges of the flow channel, it was still possible for water to leak around the bolts in the gap between the inlet and outlet channels. Plastic washers were used to eliminate leaking at the bolts.

The PIV system was deployed to acquire data in the flow planes of interest. A Flowmaster system provided by LaVision Inc. was used for data acquisition and interrogation. The system included a dual-head Nd:YAG laser as a light source, a high-resolution CCD camera, and synchronizing hardware and software. A beam expander and two cylindrical lenses with divergent angles of $f = -6$ mm and $f = -10$ mm, respectively, were utilized to create a laser sheet in the plane of interest. The camera provided a resolution of 1376 x 1040 pixels and a maximum rate of 15 frames per second. It was fitted with a 60 mm Nikon lens and a 532 nm wavelength camera filter with a bandwidth of 10 nm. Data was acquired with version 6.2.2 of LaVision's DaVis software running on a dual 2.0 GHz Intel Xeon processor computer.

A camera capture rate of 15 frames per second would only correspond to a 7.5 Hz vector field capture rate since two camera images are required per vector field. Hardware limitations further reduce the acquisition rate such that the maximum rate of the system is 4.9 Hz when capturing directly to RAM. The amount of RAM on the computer limits the number of images that can be acquired at the maximum capture rate. For this study, the first 36-40 images at each Reynolds number were taken at ~3.3Hz, with the capture rate decreasing for subsequent images.

2.2   Data Collection and Processing

In practice, fuel cell current densities commonly do not exceed 1.5 A·cm^{-2}. Above this region, which is well past the maximum power density, mass transport constraints cause the voltage to drop sharply. In a fuel cell tested in our lab, with an active area of 30 cm^2 and a channel width of 0.8 mm, the corresponding range of Reynolds numbers in the air supply channel (cathode side) was 0-2077. The flow meter used in the experiment provided flow rates which corresponded to a range of Reynolds numbers of 0-872. Data was therefore collected at flow rates ranging from 5 to 40 lph in 5 lph increments and the estimated precision of the flow meter was 1 lph. 100 pairs of images were acquired at each flow rate, with the time between pairs of images ranging from 297 ms to 3.25 seconds. At each flow rate, data was taken for the two planes of flow illustrated in Figure 2.2.

There was an observed transition in the flow pattern (elaborated upon in the results) between 15 lph and 20 lph, so additional data was collected at 17.5 lph. The data presented was collected at flow rates of 5, 10, 15, 17.5, 20, 25, 30, 35 and 40 lph. The

flow rates corresponded to Reynolds numbers of 109, 218, 327, 381, 436, 545, 654, 763 and 872 respectively.
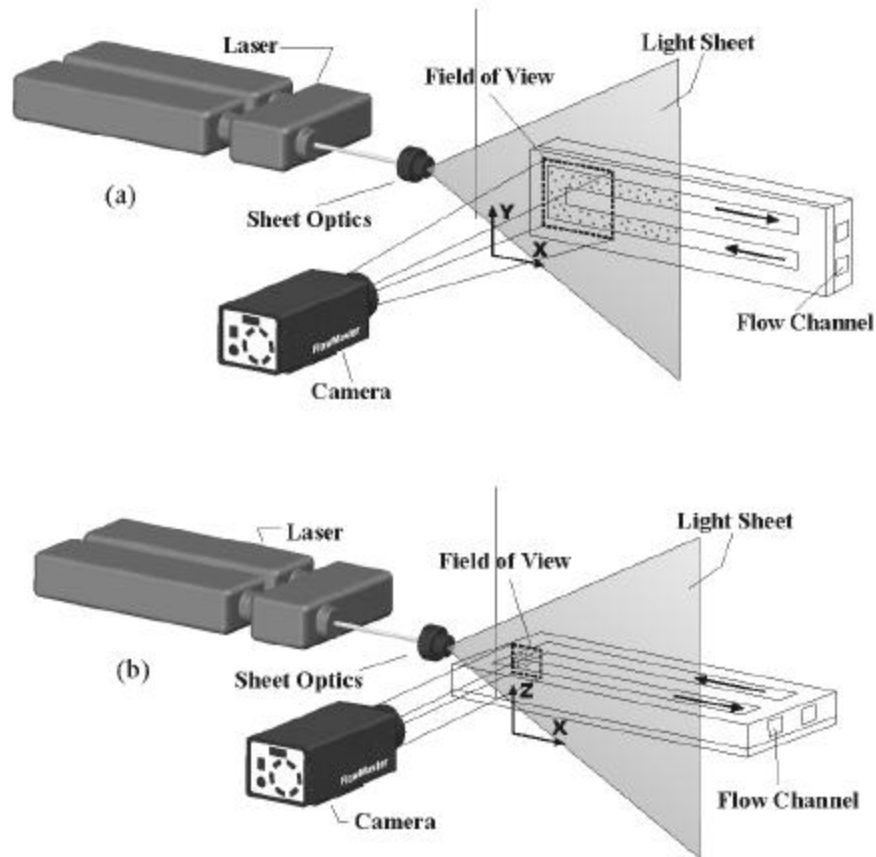
Figure 2.2: Schematic of the experimental system for acquisition of data in the (a) primary flow plane and (b) secondary flow plane.

For the purpose of calculating the Dean number, an estimation of the channel curvature was performed as shown in Figure 2.3. With a curvature ratio of 1.1, the Dean numbers for the previously mentioned Reynolds numbers are 104, 208, 312, 363, 416, 520, 624, 727 and 831 respectively. Due to the flow rate precision of 1 lph, the precision in the Reynolds and Dean numbers range from a minimum of 2.5% at the highest flow rate to a maximum of 20% at the lowest.
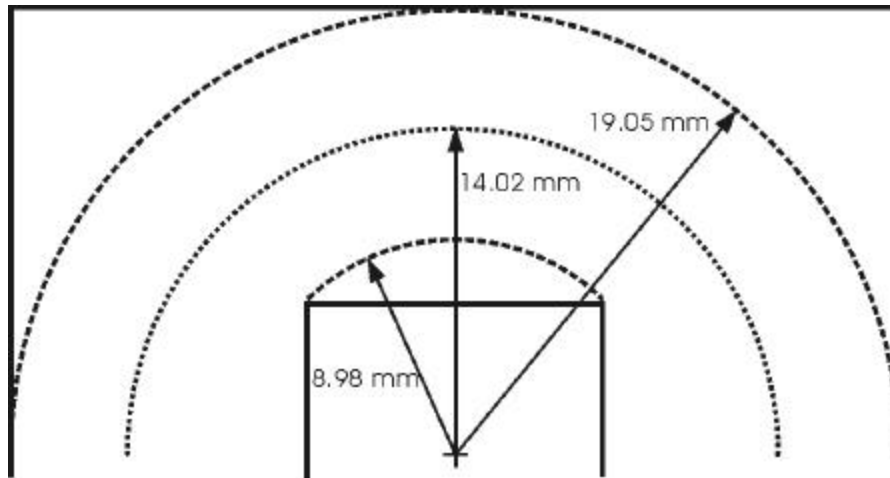
Figure 2.3: Estimation of the radius of curvature.

As shown previously, there are many techniques that can be used to increase the accuracy of PIV. Insuring proper experimental conditions (as will be addressed in section 2.2.1) can reduce the measurement error in any correlation algorithm. Additionally, proper selection of the correlation algorithm can minimize the overall error. The acquisition software provides the user with various options which implement many of the techniques described in the literature [19]. Proper selection of these options can provide accurate results for many different flows of interest.

2.2.1 Seeding of the Flow

The accuracy of PIV is directly affected by the seeding particles used since the flow velocity is estimated by the displacement of the particles. Westerweel [20] showed that the displacement field should be sampled with an average distance that is smaller than the particle displacement. Olsen and Adrian [21] proved that error due to Brownian motion can be significant at either low velocities or small seed particles. Ideal seed particles should follow the fluid flow closely without affecting the flow or interacting

with one another and should be large enough to minimize the effects of Brownian motion.

Small seed particles can also cause errors through peak locking. It can be difficult to estimate the displacement of the particles to sub-pixel resolution if the particles are too small. Peak locking error is easily detected by examining the distribution of the velocity measurements. If peak locking is an issue, the displacement measurements will be clumped around integer pixel values, rather than uniformly distributed.

The quality of the images acquired also plays a crucial role in the accuracy of PIV. Guezennec and Kiritsis [22] were the first to address the error in valid vectors. Their investigation examined the effects of different image parameters on the validity of the velocity information. Parameters such as the number of particles in the image, the mean grey level intensity of the particle pixels, the mean grey level intensity of the background pixels, the mean radius of the particles, the standard deviation of the particle radius and the standard deviation of the image noise were carefully controlled. It was determined that the dominating factor controlling the validity of the processing is the ability to separate the particles from the background.

Features of the flow can affect the accuracy of PIV as well, especially in cases of large out of plane motion and strong velocity gradients. Huang *et al.* [23] showed that these flow features can cause the particle to have a different velocity in the second image, which, in effect, distorts the second image. These deformations cause significant errors.

Studies have been conducted in attempts to limit the effects of experimental conditions. Huang *et al.* [24] proposed a computer intensive technique based on Particle Image Distortion (PID) that improved on PIV when local image deformations were large.

Meinhart *et al.* [25] presented a technique that minimized noise in images of poor quality by averaging the correlation functions prior to location of the displacement peak. Averaging the correlation function, however, eliminates the ability to resolve time-dependent flow features. With adequate attention to experimental conditions, however, it is possible to minimize the effects without adopting drastically different algorithms.

In this study, titanium dioxide particles were used since it was the seeding material provided by LaVision for use in their Flowmaster systems. While commonly used for flow measurements in combusting flows, the material can provide adequate results for water flow experiments. Dry, the particle diameter of the titanium dioxide was 200nm. When wetted, however, the titanium dioxide clumped to form particles on the order of a few µm. While the optimum particle size of just over 2 pixels was not achieved, the size of slightly over 1.5 pixels provided results with no noticeable peak locking affects.

Once the material is chosen, the two most important properties of the seeding particles are seeding density and contrast between the seeding particles and the background. Seeding density was easily controlled by slowly adding seeding particles until a desirable density was observed. Contrast between the seeding particles and the background was adjusted through modification of the laser intensity. Since 12 bit cameras were used, they could measure integer intensity levels from 0 to 4095. Increasing the laser intensity until the maximum intensity of the particles approached 4095 ensured that the contrast between the particles and the background was large. If the background intensity levels were high, there was the option to subtract it from each image. In this experiment, however, the background intensity was not an issue. Figure

2.4 shows a raw image, visualizing the seeding density and contrast of the images used for correlation.

Figure 2.4: Raw image used for calculation of the vector field.

2.2.2   Correlation Algorithm

Each algorithm is affected by imperfections in the experimental conditions differently, so while it is important to find algorithms that minimize specific experimental condition variations, it should be accomplished without the expense of attractive features such as low calculation time. There have been numerous studies over the past 10-15 years to address these issues. A few of the more notable studies are discussed.

Wereley and Meinhart [26] proposed a novel correlation algorithm using a central difference approach rather than the forward difference scheme more commonly used. By calculating the velocity at time t from data at $t - ?t/2$ and $t + ?t/2$ rather than at t and $t + ?t$, the velocity is accurate to order $?t^2$ instead of $?t$. While conceptually effective, this technique requires a complete change of the approach used. It is a possible solution for researchers seeking to write and implement their own PIV software. However, for those

looking for an accurate commercial code for quick implementation, this is not a valid option.

Hart [27] described a correlation method that can help eliminate false correlation peaks in noisy data by obtaining two correlations overlapping by 50% for each interrogation region. The two correlations are multiplied, which eliminates any correlation values not in both correlations, while amplifying any correlation values that appear in both. This method, commonly referred to as a second-order method, reduces the chance of acquiring a false vector, but produces an averaged displacement between the two correlations. In significantly noisy data, where it is difficult or impossible to reduce the noise, this is an effective approach. Conversely, other algorithms can produce higher accuracy for situations with controllable experimental conditions, where noise in the data can be limited.

Huang *et al.* [28] showed that utilizing a peak-normalization method can reduce the error in a cross correlation algorithm by almost an order of magnitude. While it was demonstrated in Huang *et al* [23, 24] that deformation caused significantly more error in PIV than their PID scheme, the difference between their scheme and a normalized PIV algorithm is minimal.

Gui and Merzkirch [29] present a Minimum Quadratic Difference (MDQ) method based on a least-square algorithm, which tracks the minimum of the quadratic difference in the gray values. It outperforms traditional correlation algorithms when a shifting interrogation window is not used. However, the results have never been compared to correlation algorithms with interrogation window shifting and the MDQ method is significantly more computationally intensive. Conventional correlation techniques

decrease computation time by instituting Fast Fourier transforms (FFT). By multiplying each pair of Fourier coefficients, Fast Fourier transforms avoid summing over all elements of the sampled region for each element. The MDQ method cannot utilize FFTs and while there is a similar technique that can be used, the affect on accuracy has never been investigated. While their results show promise, it will take more investigation to accurately gauge the potential of the MDQ method.

Two cross-correlation functions were available in the acquisition software. The first was a standard cross-correlation function utilizing a Fast Fourier transform. The basic correlation equation is defined by:

$$C(x, y) ? \sum_{x?0, y?0}^{x?n, y?n} I_1(x, y) ? I_2(x ? dx, y ? dy) \ , \ ? \frac{n}{2} ? dx, dy ? \frac{n}{2} \tag{2}$$

Where I_1 and I_2 are the image intensity of the first and second window, respectively, C is the correlation strength for all integer displacements between the two images, and n is the size of the interrogation window.

The other option was to use a normalized version of the standard function, defined by:

$$C(x, y) ? \frac{\sum_{x?0, y?0}^{x?n, y?n} I_1(x, y) ? I_2(x ? dx, y ? dy)}{RMS(I_1(x, y)) ? RMS(I_2(x ? dx, y ? dy))} \tag{3}$$

Where RMS is the standard deviation of all pixels in each of the interrogation windows.

The standard FFT correlation, which correlates at approximately a factor of 5 faster than the normalized version, was chosen for implementation with the adaptive multipass. The normalized correlation functions are most useful with varying high background intensity, which as described previously was not an issue.

Unaccounted for deformation of the particle image pattern in PIV by flow characteristics can cause large errors in PIV as shown by Huang *et al.* [23]. An alternative to the PID method described by Huang *et al.* [24] is to use a deformed second interrogation window. The iterative approach deforms the window using the particle separation in the neighboring interrogation windows obtained in the previous iteration, thus limiting the effect of particle image pattern deformation. This alternative to the PID method was used in this study.

Another option allowed for implementation of the second-order method described by Hart [26]. Erroneous vectors are usually the impetus for implementation of Hart-Algorithm at the expense of slightly larger errors in the vectors. Figure 2.5 shows an example of the original PIV vector fields prior to post-processing. Obviously erroneous vectors made up fewer than 95% of the vectors within the image; so erroneous vectors were never a major factor. Thus the increased error inherent in the Hart-Algorithm made it unattractive.
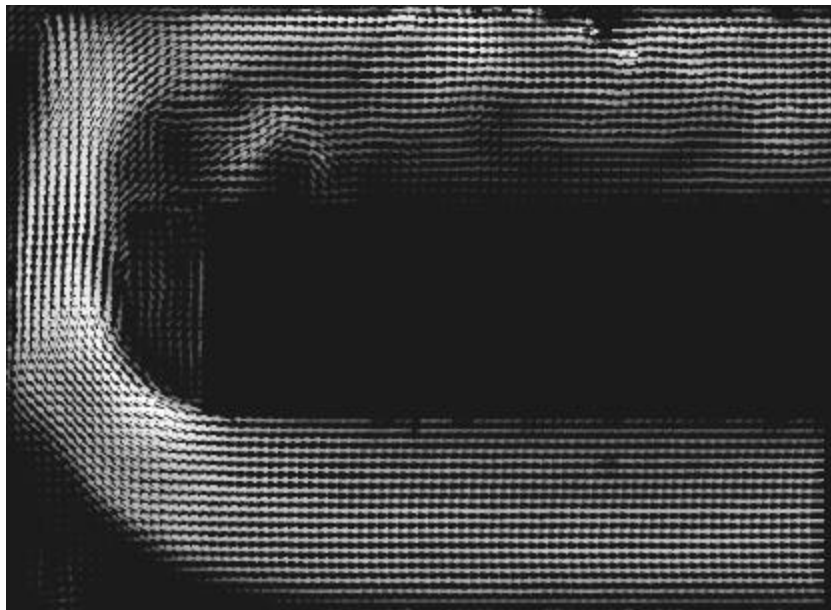

Figure 2.5: Unprocessed vector field at Re = 872.

2.2.3   Velocity Bias

Even under perfect experimental conditions, though, there will be errors in the correlation of PIV data. The two main sources of error involve the bias that algorithms have towards particular velocities. One bias, know as velocity bias, is towards low velocities. Since the likelihood of a particle from the first image leaving the interrogation region by the second image is proportional to the particles velocity, higher velocities are more likely to not be included in the correlation. The second error is sub-pixel error or peak locking as discussed earlier. Even with proper seeding, algorithms can be biased towards integer pixel displacements if the sub-pixel displacement estimation scheme is inadequate.

There have traditionally been two approaches towards minimizing velocity bias. One is to use a larger interrogation region in one image than the other, which increases the likelihood of finding a particle in the smaller of the two interrogation regions in the other. The other approach is to use interrogation regions of the same size, but which are centered at different locations. Offsetting the second interrogation region has become the favored approach because it is able to more effectively minimize velocity bias.

Westerweel *et al.* [30] were the first to examine the effect of a discrete window offset on the accuracy of cross-correlation. It was noted that the variation of the measurement error is practically independent of the displacement, except for very small displacements. The method was particularly useful to improve the signal-to-noise ratio for measurements of weak turbulence.

Scarano and Riethmuller [31] improved on this technique by instituting an iterative multigrid approach to interrogating PIV images with a discrete offset of the

interrogation window. They found that by iteratively refining the displacement of the interrogation window depending on the previously correlated displacement peak, they not only increased the maximum allowable displacement by a factor of four, they also reduced the minimum measurable displacement by a factor of three. So in addition to decreasing the bias error of the technique, they also increased the dynamic range by an order of magnitude.

An interrogation window offset was obtained by selecting an adaptive multipass option with decreasingly smaller sizes. The approach obtains the low loss of particles normally associated with large interrogation windows, while providing the high resolution of flow features associated with small interrogation windows. Two iterations were performed at a size of 64x64 pixels, adjusting the offset depending on the correlation peak. The interrogation window was then decreased to 32x32 pixels, for which an additional two iterations were performed.   The interrogation windows overlapped by 50%, yielding a grid spacing of 16 pixels and a final vector field resolution of 0.612 x 0.612 mm in the primary flow plane and 0.209 x 0.209 mm in the secondary flow plane.

Adaptive multipass also allows for restrictions on the allowable vector range. The restrictions are used to specify how much the calculated vector can deviate from the reference vector used for the previous offset. Relative and absolute restrictions can be used independently or together. The relative vector range restriction, of reference ± window size/3, was used in addition to an absolute vector range restriction of reference ± 5 pixels.

2.2.3.1   Sub-pixel Error

Sub-pixel estimation schemes are the leading method for minimizing sub-pixel error. There are various techniques that use the expected intensity profile of the seeding particles to estimate the center of each particle. Errors in the method used to extract the displacement peak from the correlation function result in the errors in the displacement calculation.

Forliti *et al.* [32] compared several different methods for estimating the displacement peak location to a sub-pixel level. These methods included Parabolic curve-fit, Gaussian curve-fit, the Centroid method and Whittaker's reconstruction. While all algorithms tended to bias the displacements towards the nearest pixel value, they found that in general, the Gaussian curve-fit algorithm had the lowest bias and precision errors. With the use of a correction, the error in Whittaker's reconstruction can be reduced to that of the Gaussian curve-fit.

Other researchers have also noted the findings of Forliti *et al.* as well. Willert and Gharib [33] examined the implementation of a three-point estimation technique for locating the correlation peak. Lourenco and Krothapalli [34] recommended the Gaussian peak interpolator and the Whittaker's interpolator for sub-pixel accuracy.

One of the only studies in predicting the sub-pixel error is Westerwel [35]. He derived an analytical expression for the error in estimating the sub-pixel displacement. It was demonstrated that oversimplification of the image properties in generating synthetic PIV images for Monte-Carlo simulation studies systematically underestimates the measurement error for PIV. While it was shown that the error in sub-pixel displacements

are higher that commonly reported, this would not affect the relative errors of the various estimation methods.

For this study, a three-point Gaussian peak fit was used, with two independent two-dimensional Gaussian functions fitted to the correlation peak in the x- and y-direction.

2.2.4 Vector Filtering

When using multipass windowing with an adaptively adjusted window-shift it is important that the vector field contain as few spurious vectors as possible [19]. As the window is decreased, it is essential to detect any false vectors in the intermediate steps, even at the expense of some valid vectors. For this reason, a strong median filter was used at each step. Additionally, this particular filter was applied to the final vector field during post-processing. The algorithm, a four pass method, is similar to that presented by Nogueira *et al.* [36]. The first pass eliminated all vectors that were greater than 2.5 times the RMS of its neighbors. The second pass eliminated all vectors that had fewer than 3 neighbors. The third pass is an iterative procedure that tries to insert as many good vectors as possible that are less than 2.5 times the RMS of the neighbors. Up to three lower correlation peaks are checked as well as the highest correlation peak. The process is repeated until no more new vectors can be filled in. The final pass removes any groups with an insufficient number of vectors.

An additional criterion used for false vector detection was the peak ratio, defined as:

$$Q ? \frac{P1 ? \min}{P2 ? \min} ? 1 \tag{4}$$

Where P1 and P2 were the heights of the first and second highest correlation peaks and min was the lowest value of the correlation plane, which corresponded to the common background correlation. If the peak ratio for an interrogation window was less than 1.5, the vector was removed.

Smoothing was performed after the entire vector field was correlated as fully as could be achieved. All empty spaces were filled with an average of all non-blank neighbors. The process was repeated until no more interpolated vectors were added.

2.2.5 Derived Flow Characteristics

Velocity is not the only flow characteristic that is of interest to experimentalists. There are several important characteristics that can be derived from the velocity field and errors are present in the estimation of each. For instance, the errors in vorticity stem from two sources: errors within and implementation of the vorticity calculation scheme and errors in the velocity data used for the vorticity calculation. While other derived characteristics such as RMS and Reynolds stress have similar error sources, the errors in vorticity can be particularly high. Vorticity is most commonly derived from the variations between the velocity at the location of interest and that of its neighbors. Since the variations between velocities of neighboring interrogation regions will be small, vorticity calculations are particularly sensitive to errors in the velocity calculation. Due to the relatively high errors that can be associated with vorticity, it has received significant attention in the literature.

Vorticity is most commonly calculated by estimating the velocity derivatives. While there have been several studies investigating the errors associated with calculating the velocity derivatives, most studies have looked to alternate techniques to minimize the

error. One of the notable exceptions is Lourenco and Krothapalli [34], who present a scheme for computation of velocity derivatives that differed from the common schemes at the time. While Huang *et al.* [23] did not present an alternate approach for vorticity calculation in their study of PIV error due to deformation, they did examine the effects of deformation on the vorticity. Of the investigations into alternate approaches, several are notable.

Ruan *et al.* [37] analyzed vorticity error using the velocity data in an estimation scheme. It was noted that the smaller the grid size, the lower the bias error, but the higher the uncertainty. In general, the higher the order of the scheme, the lower the bias error, but the sensitivity to velocity measurement uncertainty increases. They developed a technique called direct measurement of vorticity (DMV), which determines vorticity directly from the average angular displacement of rotation between two matched patterns.

Nogueira *et al.* [36] investigated derived magnitude calculation from PIV data and the effects of invalid vectors. They noted that the existence of false vectors deteriorates the quality of the results as it increases the difficulty in their interpretation and sometimes precludes obtaining derived flow magnitudes.

Abrahamson and Lonnes [38] suggested a least-squares approach to vorticity calculation, but it was found to only be useful if the velocity is randomly spaced or the character of the vorticity field is more important than the magnitude.

Similar to the alternative approaches for correlation algorithms, these alternate vorticity calculation approaches are more useful for researchers looking to implement their own PIV code rather than those looking to quickly implement a proven code to a particular situation of interest.

In this study, the vorticity, RMS and Reynolds stress were all calculated where applicable. The vorticity and root-mean square (RMS) were calculated within The acquisition software, while the Reynolds stress was calculated externally.

Vorticity is a measure of the rate of rotational spin in a fluid. It can be useful in characterizing mixing as well as flow separation and reattachment. For the primary and cross-plane vorticity, ω_z and ω_y respectively, the vorticity was calculated from Equations 5 and 6.

$$\omega_z \approx \frac{\partial v}{\partial x} - \frac{\partial u}{\partial y} \approx \frac{\overline{v}_{x_1} - \overline{v}_{x_2}}{x_1 - x_2} - \frac{\overline{u}_{y_1} - \overline{u}_{y_2}}{y_1 - y_2} \tag{5}$$

$$\omega_y \approx \frac{\partial w}{\partial x} - \frac{\partial u}{\partial z} \approx \frac{\overline{w}_{x_1} - \overline{w}_{x_2}}{x_1 - x_2} - \frac{\overline{u}_{z_1} - \overline{u}_{z_2}}{z_1 - z_2} \tag{6}$$

Where v is the y-component of velocity, u is the x-component of velocity and w is the z-component of velocity. The subscripts 1 and 2 are neighbor positions of the vector in question. Preferably the vectors to the top (and to the right) are used. However, if those vectors are not present (empty or at the image rim) the bottom (and the left) vectors are used.

The averaged fluctuation amplitude of the separated flow in the U-bend is commonly characterized by patterns of root-mean-square (RMS) velocity fluctuations $|\underline{V}|_{rms}$. The acquisition software calculated the RMS component by component, from which the magnitude of the RMS was calculated using an algorithm. The x-component of the RMS was calculated as shown in Equation 7, as were the y- and z-components.

$$|V|_{rms} \; ? \; \sqrt{\frac{n \, ? \, _i x_i^2 \, ? \, ? \, _j x_j^2}{n \, ? n \, ? \, 1 \, ?}}$$ (7)

Where n is the number of source files at each Reynolds number.

The level of turbulent activity and mixing is often characterized by the Reynolds stress correlation <u?v?>, where u? and v? are the *fluctuating* velocity components in the x- and y-directions. Since the acquisition software did not calculate the Reynolds stress an algorithm was written to implement Equations 8 and 9.

$$? \, u ? v ? ? ? \; \frac{1}{n} \, ?_{i?1}^{n} \, ? u_i \, ? \, ? \, u \, ? \, ? ? ? v_i \, ? \, ? \, v \, ? ?$$ (8)

$$? \, u ? w ? ? ? \; \frac{1}{n} \, ?_{i?1}^{n} \, ? u_i \, ? \, ? \, u \, ? \, ? ? ? w_i \, ? \, ? \, w \, ? ?$$ (9)

Where < > denotes an averaged quantity.

2.2.6   Additional Data Processing

In addition to calculating quantities that weren't available through the acquisition software, algorithms were written for combining multiple data files into single files for graphing. It would have been possible to accomplish everything manually, but the shear number of files (over 7000) made manual manipulation impractical. Simple algorithms were constructed to manipulate the data files and adjust parameters for ease of presentation. Some files had to be reorganized to match the formatting of other files, magnitudes of computed quantities were calculated, the coordinate systems were adjusted to ease interpretation and formatting for graphical representation was added.

CHAPTER 3   RESULTS

The experimental data indicates the presence of two main flow regimes. The flow pattern at Re = 381 are drastically different from the flow patterns at Re = 436. At each flow rate, in the low Reynolds number regime, the velocity vector field, out-of-plane vorticity contours, and streamlines are consistent for the entire data set. Examination of the averaged (over the entire data set) and instantaneous flow fields both flow regimes clearly illustrate the consistencies or inconsistencies in the flow. In the lower Reynolds number regime, the averaged flow fields are almost identical to the proceeding instantaneous flow fields. Contrarily, the instantaneous flow field can bear little resemblance to the averaged flow field at higher Reynolds numbers.

There are two sections of data, one corresponding to the primary flow plane and one for the secondary flow plane. Additionally, each section is separated into the lower Reynolds number regime and the higher Reynolds number regime. Each figure contains the velocity vector field, the out-of-plane vorticity contours and the velocity streamlines. In the out-of-plane vorticity contours the positive vorticity represents counter-clockwise rotation, while the negative vorticity represents clockwise rotation. The light gray regions represent locations where no data is available due to optical inaccessibility.

3.1   Primary Flow Plane

The primary flow plane is the data collected in the experimental configuration shown in Figure 2.2(a). The fluid enters the U-bend on the bottom of the image from right to left and then exits the U-bend at the top of the image from left to right. Averaged

figures contain the average of all 100 pairs of images taken at each of the Reynolds numbers.

3.1.1 Pre-Transition Flow Patterns

Data was acquired at 4 Reynolds numbers prior to the transition regime. At Re = 109, 218, 327 and 381, the flow contains the features associated with the low Reynolds number regime. Only data at Re = 109 [Figure 3.1] and Re = 381 [Figure 3.2] is presented. Data for the additional Reynolds numbers can be found in Appendix A. Little or no fluctuation is detectable in this low-flow-rate regime. Each of the instantaneous images is essentially identical to the time-averaged flow representations, indicating steady flow conditions.

In the velocity vector field, one can observe the low-velocity region near the top corner of the U-bend. It shows an area where the velocity near the centerline of the channel is significantly lower than the surrounding fluid. This is the most distinctive feature of the vector field at low Reynolds numbers. Another feature involves a recovery of the laminar velocity profile. When the fluid approaches the U-bend, the flow contains an approximately parabolic laminar flow profile with the maximum along the centerline of the channel. As the flow moves through the U-bend, the flow near the centerline of the flow reduces in relationship to the surrounding fluid. In the return channel, however, the velocity along the centerline of the channel approaches that in the entrance region.

Additionally, the vorticity contour plot demonstrates the effect of the U-bend on vortex formation. As expected, the first and second edges of the U-bend induce vortices. Although not as clear at Re = 109, a shear layer (represented by neighboring counter-rotating vortices) corresponding to the low-velocity region can also be seen near the

second edge as the strong vortex induced by the first edge splits into two smaller scale vortices, of which one reattaches prior to the second edge. Between the images at Re = 109 and Re = 382 the point of reattachment moves farther up vertical section along the inside of the U-bend. The flow recovery is also illustrated by the out-of-plane vorticity contours. In the return channel, like in the entrance channel, there are very few small-scale vortices in the bulk of the fluid. Instead, vortices are confined mainly to the upper and lower walls of the channel.

If the out-of-plane vorticity contour in Figure 3.2(a) is examined closely, one can notice two small circular counter-rotating vortices in the top right corner near the exit of the flow. These are erroneous values caused by a single particle stuck to the Plexiglas lid of the flow channel. The single particle reflected enough light to contaminate the velocity data sufficiently to produce the false vortices. While the other images affected by this were corrected, this particular image was kept to illustrate, as commented upon in the literature, the error propagation in vorticity due to erroneous velocity vectors.

The velocity streamline plot gives insight into the general flow of the fluid. The most obvious effects on flow occur in the outer corners and inner wall of the U-bend and oftentimes a single circulation zone can be seen at one of the two corners. Impingement of the velocity on the outer wall of the U-bend, as well as along the return channel, is clearly shown. As the Reynolds number increases, gradually the impingement of the flow does as well.
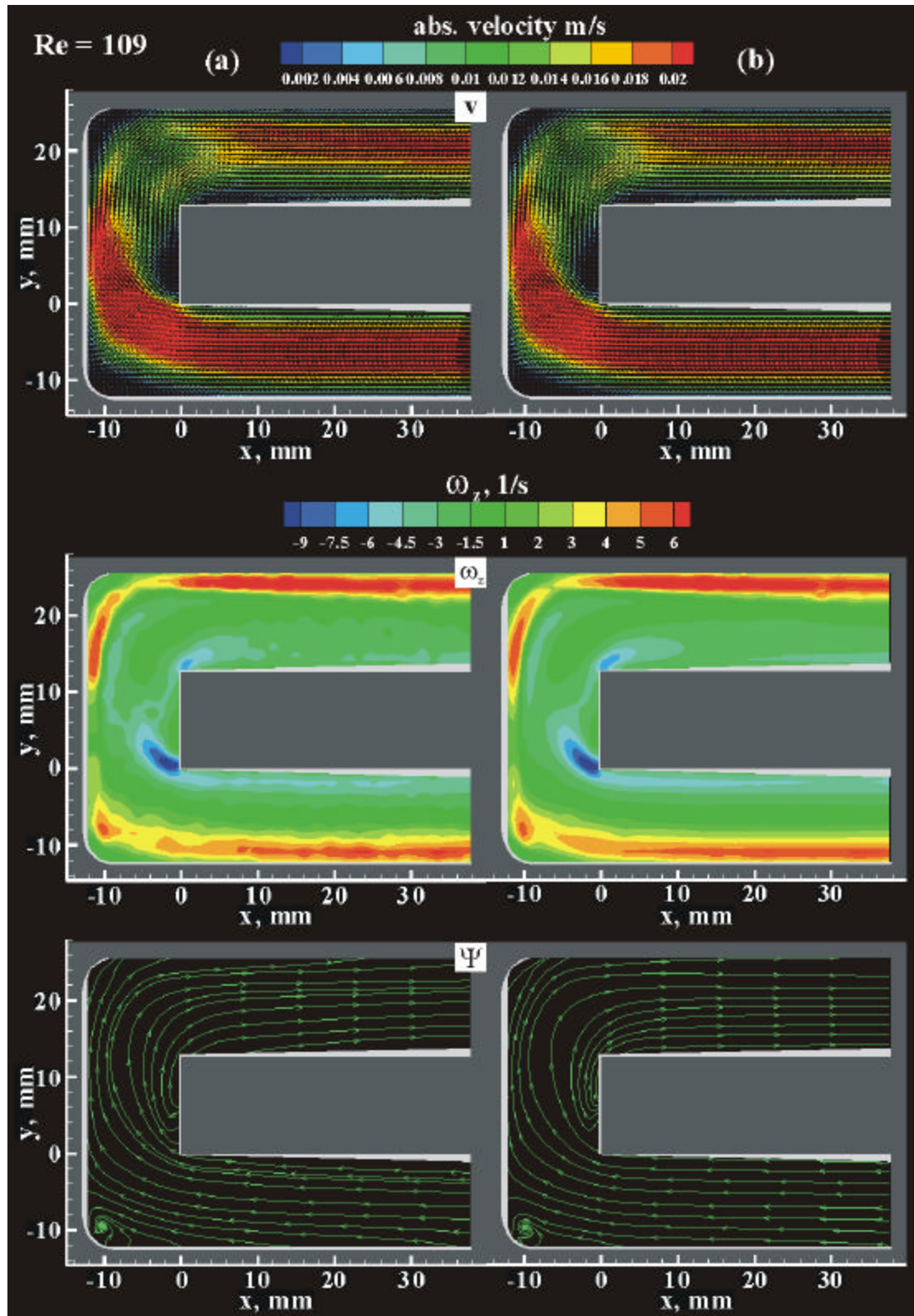
Figure 3.1: (a) Instantaneous and (b) averaged flow fields for the primary flow plane at Re = 109. From top to bottom: velocity vector field; out-of-plane vorticity contours; velocity streamlines.
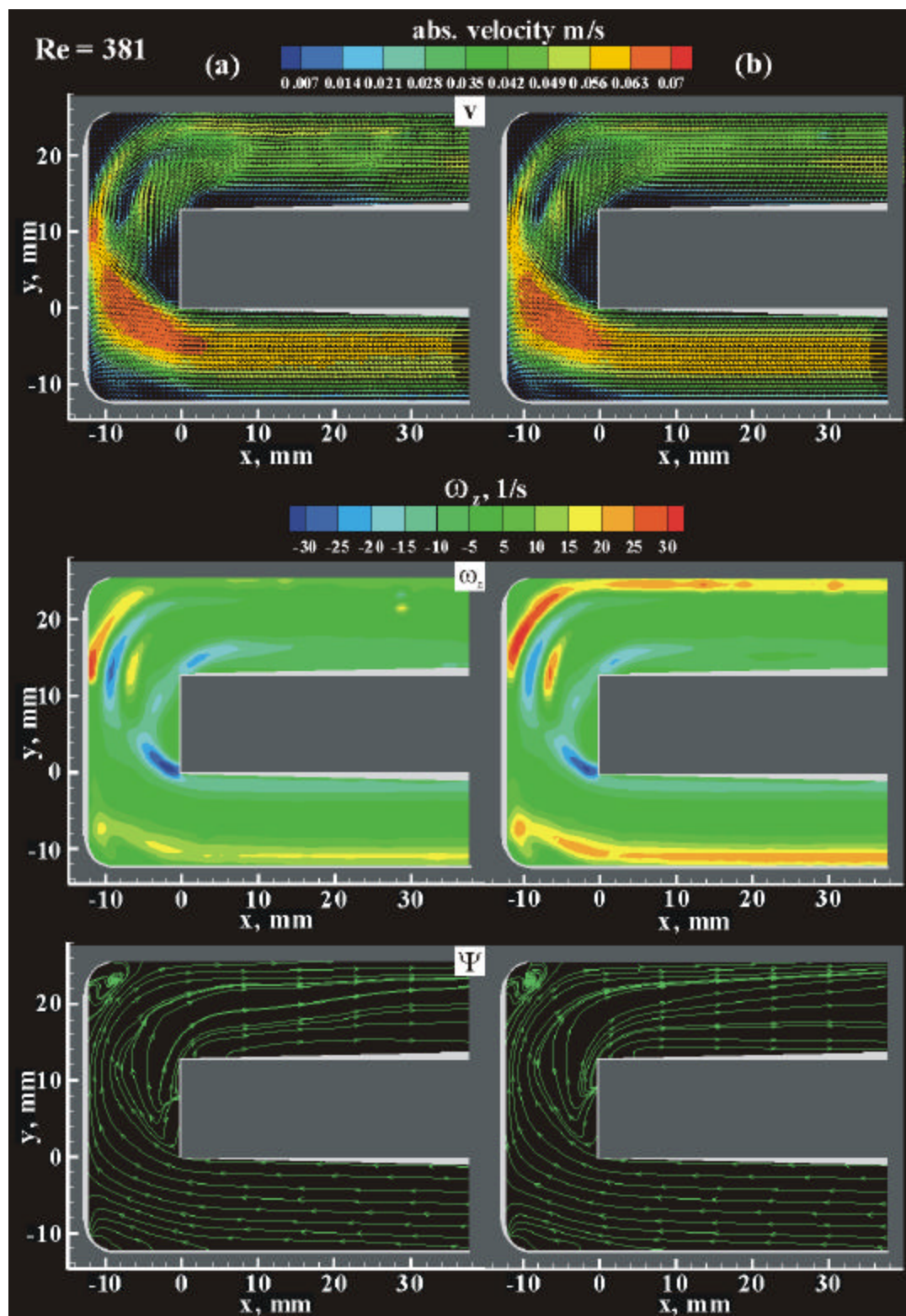
Figure 3.2: (a) Instantaneous and (b) averaged flow fields for the primary flow plane at Re = 381. From top to bottom: velocity vector field; out-of-plane vorticity contours; velocity streamlines.

3.1.2 Post-Transition Flow Patterns

Five sets of data after the transition were collected at Re = 436, 545, 654, 763 and 872. Data at Re = 436 and Re = 872 are presented here [Figure 3.3 and Figure 3.4 respectively], while data for the other sets is in Appendix A. In each figure, the plots from left to right are the velocity vector field, out-of-plane vorticity contours and velocity streamlines. While the flow patterns still exhibit global features of the pre-transition flow, the flow becomes unsteady after the transition. Unsteadiness is manifested primarily in the variation of the large-scale flow structures of the instantaneous images, Figure 3.3(a)-(c) and Figure 3.4(a)-(c). The unsteady nature of the flow is also illustrated by a comparison of the instantaneous images and the averaged images, Figure 3.3(d) and Figure 3.4(d). It should be noted that the scales used for the pair of figures at each Reynolds number are the same. The same scale is used to clarify the magnitudes of the common flow features for easy comparison.

Variations in the flow can clearly be seen in the velocity vector fields, especially that there is no longer the consistent exit flow along the radius of curvature. Unsteadiness is manifested in the shrinking, expansion, and disappearance of the low-velocity region. After the transition, unlike at the low flow regime, the flow does not recover quickly after the U-bend. The maximum velocity is along the upper wall of the return channel and remains there for the remainder of the visualized area.

The out-of-plane vorticity contour plots best illustrate the unsteadiness of and instabilities within the flow after the transition. As prior to the transition, vortices are induced at the first and second edges of the U-bend. Unlike prior to the transition, however, the existence of the shear layer (corresponding to the low-velocity region) from

the flow separation caused by first edge is inconsistent. It only appears in images with a corresponding low-velocity region in the velocity vector field. Additionally, the flow separation at the first edge of the U-bend does not reattach prior to the second edge. This is the cause of the unsteadiness observed in the flow and is illustrated by the variation between the averaged images and the instantaneous images. It can also be observed in the region of the flow separation and the U-bend that the number and scale of the small-scale vortices increases with increasing Reynolds number.

The vorticity of the instantaneous figures clearly shows the instabilities downstream from the U-bend. Smaller scale vortices in the bulk stream of the return channel describe a flow that contains significantly more rotational spin than it did prior to the U-bend. In the entrance channel the vortices are confined mainly to the upper and lower walls, similar to the low Reynolds number regime. In the return channel, however, the vortices are no longer confined to the walls.

Again, the velocity streamline plot gives insight into the general flow of the fluid at each Reynolds number. As prior to the transition, the most obvious effects on flow occur in the outer corners and inner wall of the U-bend. After the transition, however, the flow effects at these locations are almost always in the form of a circulation zone. In some cases, multiple circulations zones are visible. Another characteristic unique to flows after the transition are circulation zones that can sometimes be seen along the lower wall of the return channel. Impingement of the velocity on the outer wall of the U-bend, as well as along the return channel, is also seen after the transition but quantitatively more significant than prior to the transition.
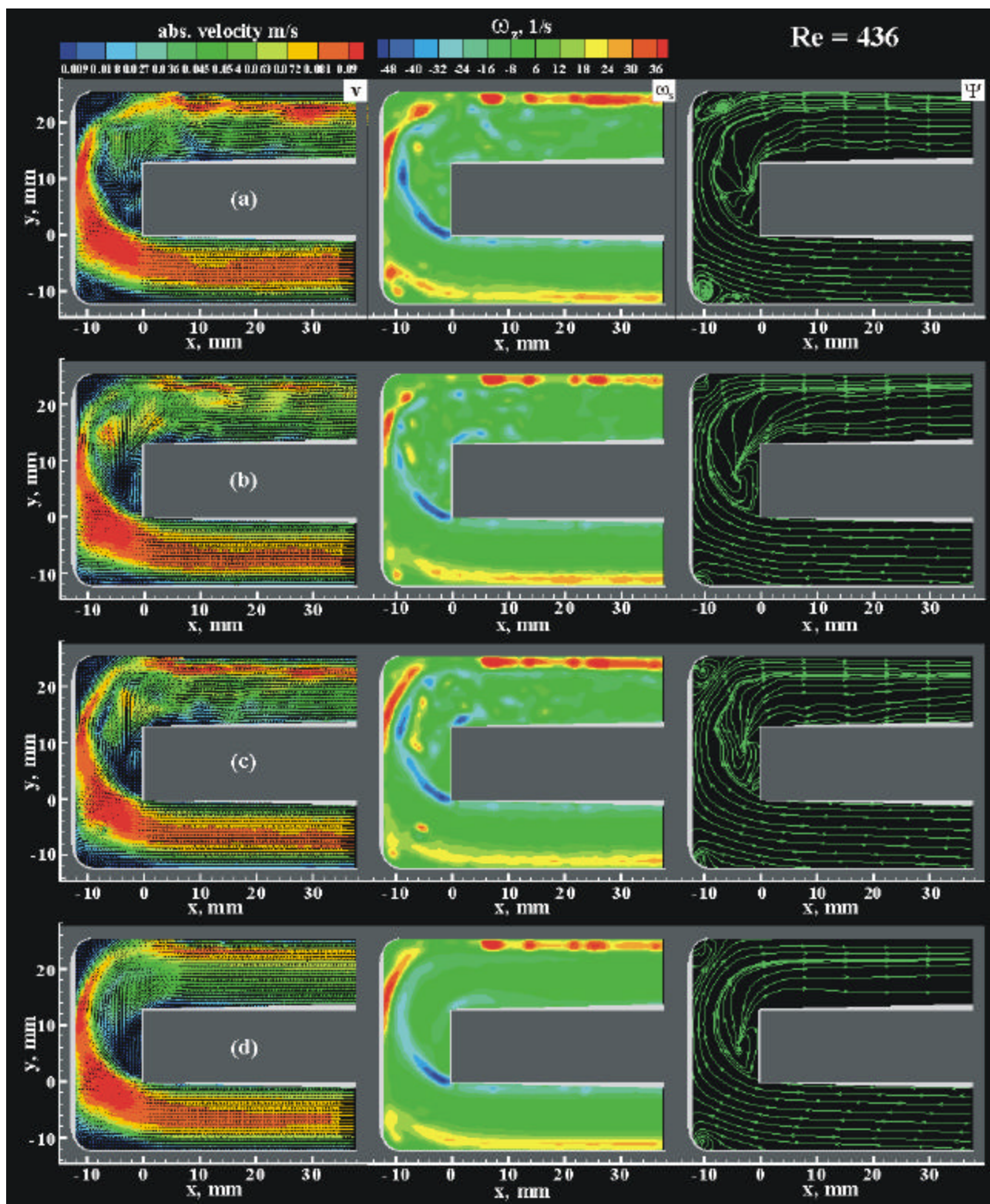
Figure 3.3: (a), (b), (c) Instantaneous and (d) averaged flow fields for the primary flow plane at Re = 436. From left to right: velocity vector field; out-of-plane vorticity contours; velocity streamlines.
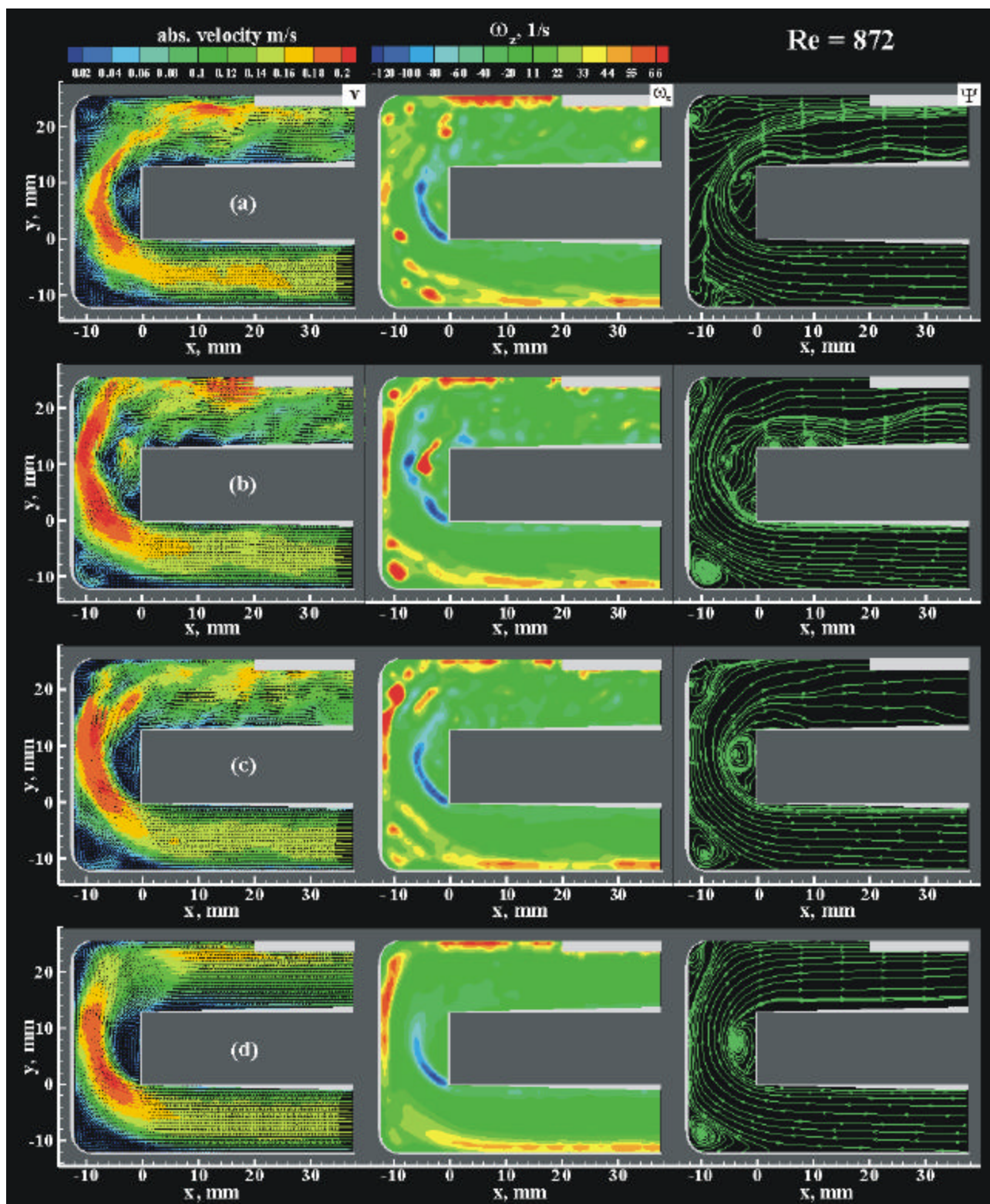
Figure 3.4: (a), (b), (c) Instantaneous and (d) averaged flow fields for the primary flow plane at Re = 872. From left to right: velocity vector field; out-of-plane vorticity contours; velocity streamlines.

3.2   Secondary Flow Plane

The complexity of the structures, as well as the well-documented characteristics of Dean type flow, suggested that significant secondary motion in the U-bend should be expected.   Data was acquired at a second plane of view to investigate the symmetric circulation zones and any additional secondary motion.   The second plane of view was perpendicular to the first and located at the center of the U-bend.   As previously discussed, the secondary flow plane was as illustrated in Figure 2.2(b).

For the figures of the secondary flow plane, as with the primary flow plane, an average of the 100 images acquired at each Reynolds precedes a representative instantaneous image.   The primary flow through the channel is directed towards the reader.   Again, the gray areas represent regions where data is unavailable due to optical inaccessibility.   Unlike the primary flow plane, the size of the unresolved area in the secondary flow plane is significant.   The inaccessible region on the right side of each plot is caused by the curvature of the outside corners of the U-bend produced in the machining process.   On the bottom of each plot, there is an inaccessible region resulting from the outer seal of the channel.

3.2.1   Pre-Transition Flow Patterns

Figure 3.5(a) and Figure 3.6(a) contain instantaneous flow data in the secondary flow plane for Re = 109 and Re = 381 respectively, while Figure 3.5(b) and Figure 3.6(b) contain averaged flow data.   As with the primary flow plane images, one of the most obvious features of the low Reynolds number regime is the similarity between the

averaged and instantaneous flow data. Additional visualizations for the remaining pre-transition Reynolds numbers are contained in Appendix B.

Two major symmetric circulation zones are present in the velocity vector field prior to the transition. These are expected from previous studies and have been experimentally verified in the past. Unfortunately, since one of the inaccessible regions is along the outer edge of the channel, it is impossible to determine if the 4- and 6-vortex structures are ever present.

The out-of-plane vorticity plot confirms the existence of the main vortices as well. Increasing Reynolds number leads to significantly higher values of circulation in the Dean vortices and the formation of additional smaller scale vortices. While indicating the onset of instability, these small-scale vortices are quite symmetric and low in magnitude prior to the transition to unsteadiness. The major vortices tend to become more circular with increasing Reynolds number, while the secondary vortex along the top elongates. This is most likely an affect of the increase in the centrifugal force at higher velocities.

In the secondary flow plane, the velocity streamlines oftentimes give the most insight into the structure of the secondary flow with their clear visualization of circulation zones. At Re = 109 there are only two circulation zones, which are clearly symmetric. These two circulation zones are present and similar in both the averaged and instantaneous figures. However, at Re = 381, additional circulation zones are present along the inner wall in both the averaged and instantaneous images. A close symmetry is maintained in these smaller scale circulation zones as well.
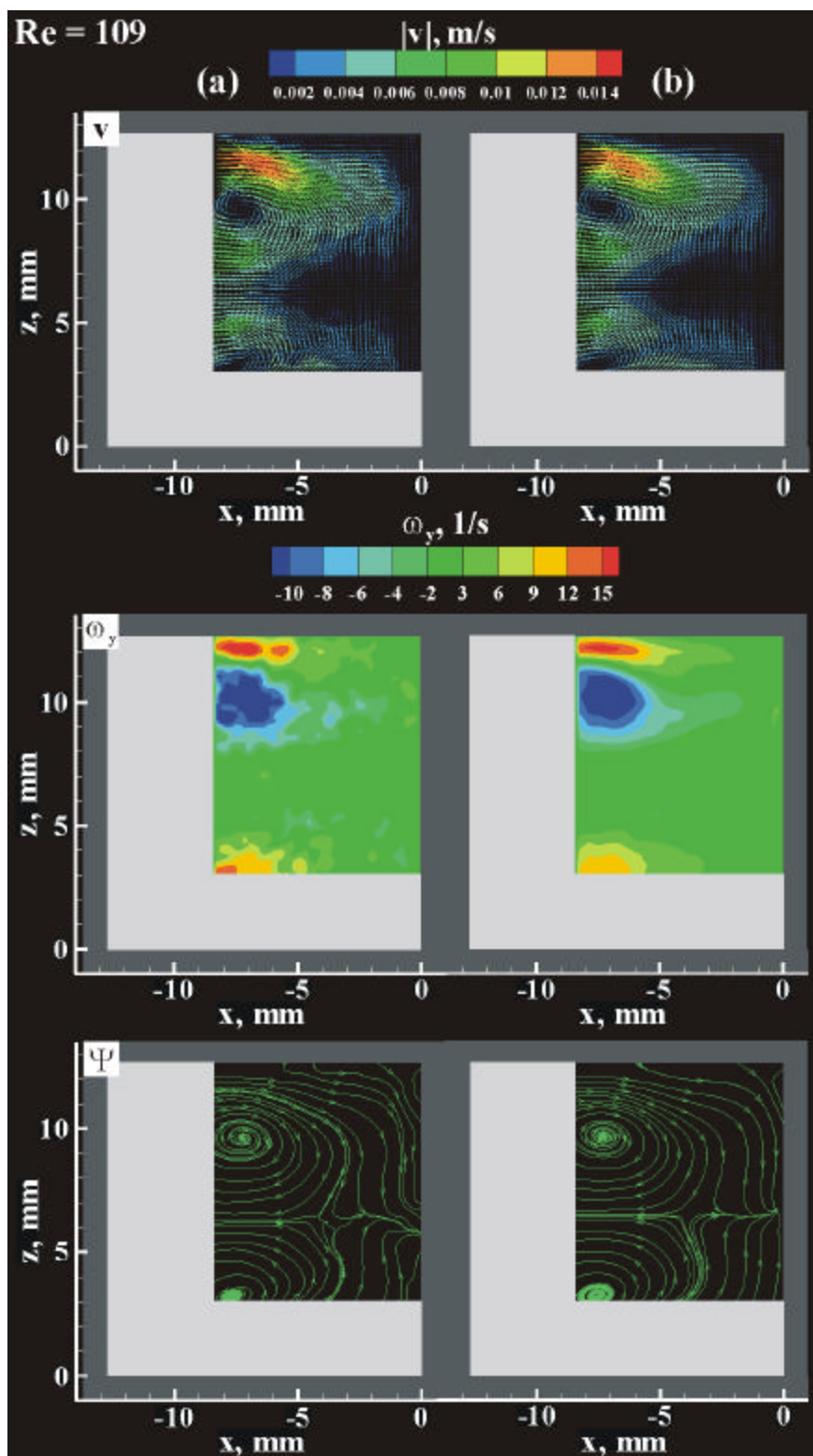
Figure 3.5: (a) Instantaneous and (b) averaged flow fields for the secondary flow plane at Re = 109. From top to bottom: velocity vector field; out-of-plane vorticity contours; velocity streamlines.
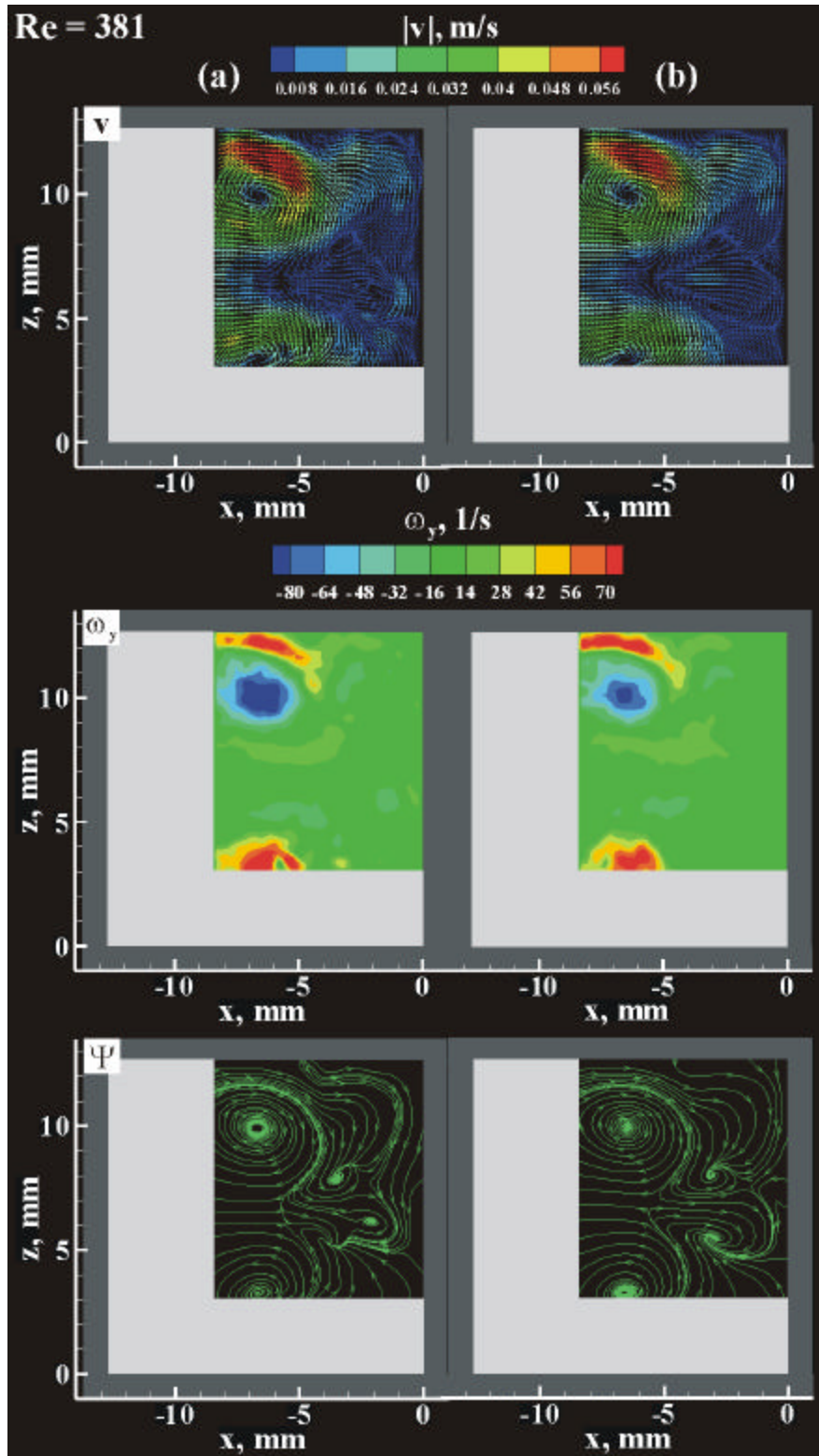
Figure 3.6: (a) Instantaneous and (b) averaged flow fields for the secondary flow plane at Re = 381. From top to bottom: velocity vector field; out-of-plane vorticity contours; velocity streamlines.

3.2.2   Post-Transition Flow Patterns

As in the primary flow plane, the flow in the secondary flow plane is unsteady after the transition.   The variations can still be seen between the individual instantaneous images at Re = 436 [Figure 3.7(a)-(c)] and Re = 872 [Figure 3.8(a)-(c)] as well as between the instantaneous and averaged data [Figure 3.7(d) and Figure 3.8(d)].   In the secondary plane, however, the variations are even more pronounced.   Again, the scales used for the pair of figures at each Reynolds number are the same.   In the secondary plane the differences in magnitudes of velocity and vorticity between the average and instantaneous images can be quite large.   Appendix B contains flow representations from the additional Reynolds numbers.

While the averaged velocity vector plots are quite similar to the images prior to the transition, the instantaneous plots are not.   After the transition, three or more small-scale regions of circulation can replace the two main small-scale circulation regions common prior to the transition.   The stronger fluctuating Dean vortex pair induces these smaller-scale vortices, in which symmetry is less common than in the low-flow-rate regime.   Instead, they appear intermittently throughout the flow field and exhibit a range of scales and circulation values due to mutual induction as well as the interaction with the Dean vortices and the channel walls.

As with the velocity plots, the averaged out-of-plane vorticity plots after the transition are similar to those prior to the transition.   The general trend is for the major vortices to be pushed towards the sidewalls and develop a more elliptical than circular shape.   Most likely this is an affect of the increasing velocities corresponding to higher centrifugal forces.   In the instantaneous images the number of secondary vortices

increases along with their magnitude until they are on the order of the major vortices seen in the averaged images. The location and shape of the vortices becomes random and symmetry is commonly lost.

Many of the same features are commonly seen in the streamlines, which, as with the pre-transition images provide good insight into the structure of the secondary flow. Even in the averaged data, symmetry can sometimes be lost. A clear trend in the averaged data with increasing Reynolds number is often unavailable. Sometimes there are secondary circulation zones along the inner edge and sometimes there aren't. In the instantaneous images, the general trend is towards more chaotic flow. In some cases, Figure 3.7(a), the secondary cells along the inner edge are present, just slightly shifted. In others, Figure 3.7(b),(c) and Figure 3.8(a)-(c), there is not only a lack of symmetry but a lack of an organized structure as well.
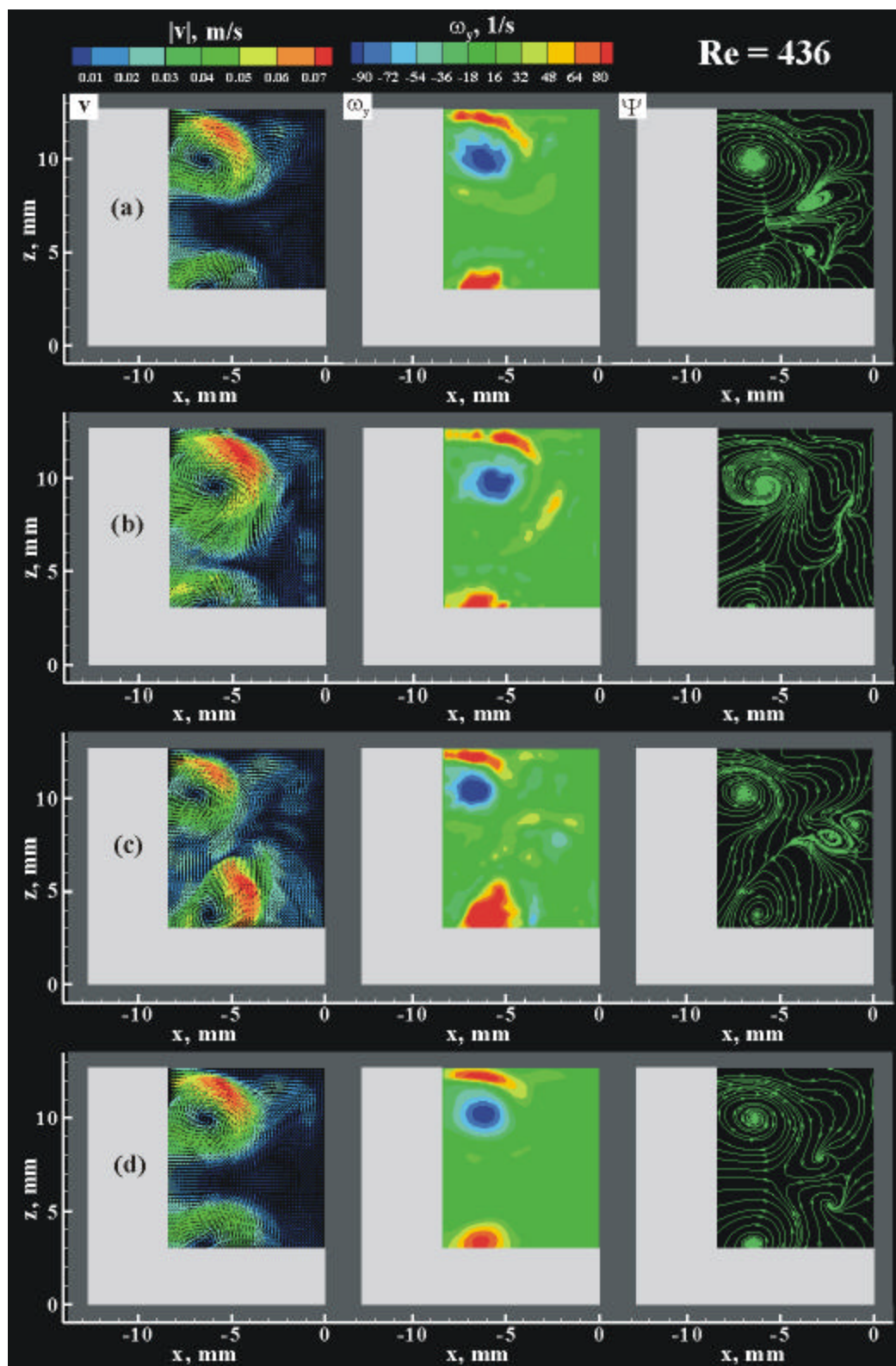
Figure 3.7: (a), (b), (c) Instantaneous and (d) averaged flow fields for the secondary flow plane at Re = 436. From left to right: velocity vector field; out-of-plane vorticity contours; velocity streamlines.
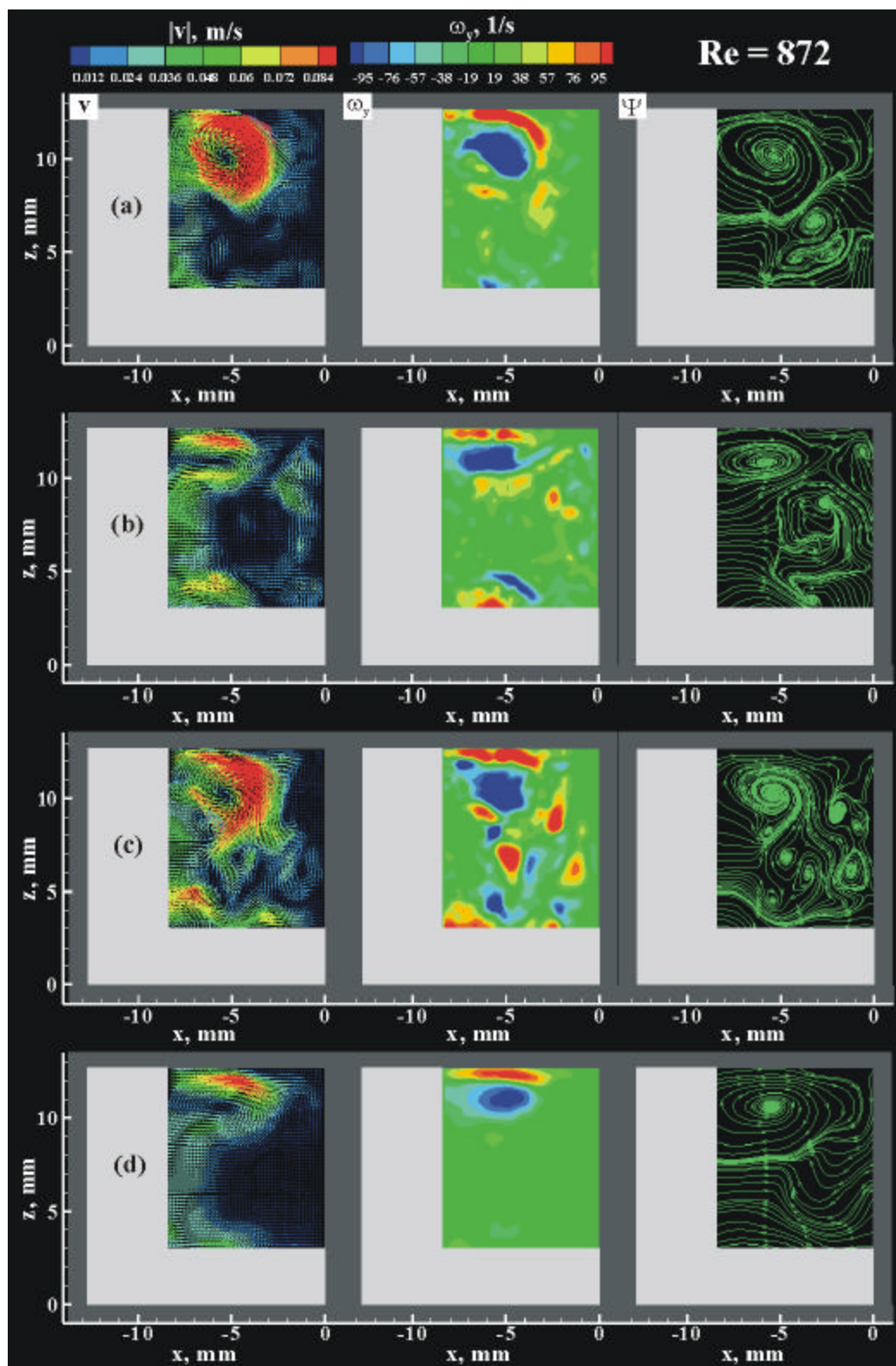
Figure 3.8: (a), (b), (c) Instantaneous and (d) averaged flow fields for the secondary flow plane at Re = 872. From left to right: velocity vector field; out-of-plane vorticity contours; velocity streamlines.

3.3 Properties of Unsteadiness

It is desirable to attempt to characterize the unsteadiness in a manner that provides further insight into the observed phenomena. RMS, Reynolds stress and oscillation frequency were the quantities chosen for this characterization. Equations 7, 8 and 9 from Section 2.2.6 were used to compute the RMS and Reynolds stress respectively. Both quantities were calculated for each post-transition Reynolds number as well as at Re = 381 to give a comparison to the pre-transition quantities. Since both the RMS and Reynolds stress are measures of unsteadiness, it was correctly expected that they would have negligible magnitudes in the pre-transition regime. Any measurable values of the RMS and Reynolds stress were most likely noise in the data rather than relevant features of the flow. Additionally, to provide clear comparisons, each individual plot within each figure contains the same scale.

3.3.1 RMS

Figure 3.9 shows distribution of $|\underline{V}|_{rms}$ in the primary flow plane for six different values of Reynolds number. For the lower flow rates (Re < 381), the flow is essentially steady, and no significant velocity fluctuations were detected. As the Reynolds number increases, the fluctuations become more pronounced, and the $|\underline{V}|_{rms}$ magnitudes increase. The highest values are associated with the recirculation zones at the outer corners of the U-bend and with the separated flow region originating from the first (downstream) inner corner. At the higher flow rates (Re = 763 and Re = 872), flow oscillations in the channel downstream of the U-bend can be observed. In this region, the local peak of the $|\underline{V}|_{rms}$ values corresponds to the re-attachment of the flow to the inner wall.

Patterns of root-mean-square velocity fluctuations in the secondary flow plane are shown in Figure 3.10. Similarly to the primary flow plane, the amplitude of the oscillations increases with increasing flow rate. This is manifested by the increase in the peak values of $\underline{V}|_{rms}$. The highest magnitudes correspond to the counter-rotating Dean vortices. Although these vortices remain the dominant feature of the secondary flow patterns, their location and shape fluctuate as the Reynolds number increases. Moreover, the smaller-scale secondary vortices that appear intermittently at higher flow rates contribute to the increase of the $|\underline{V}|_{rms}$ levels in the secondary flow plane.
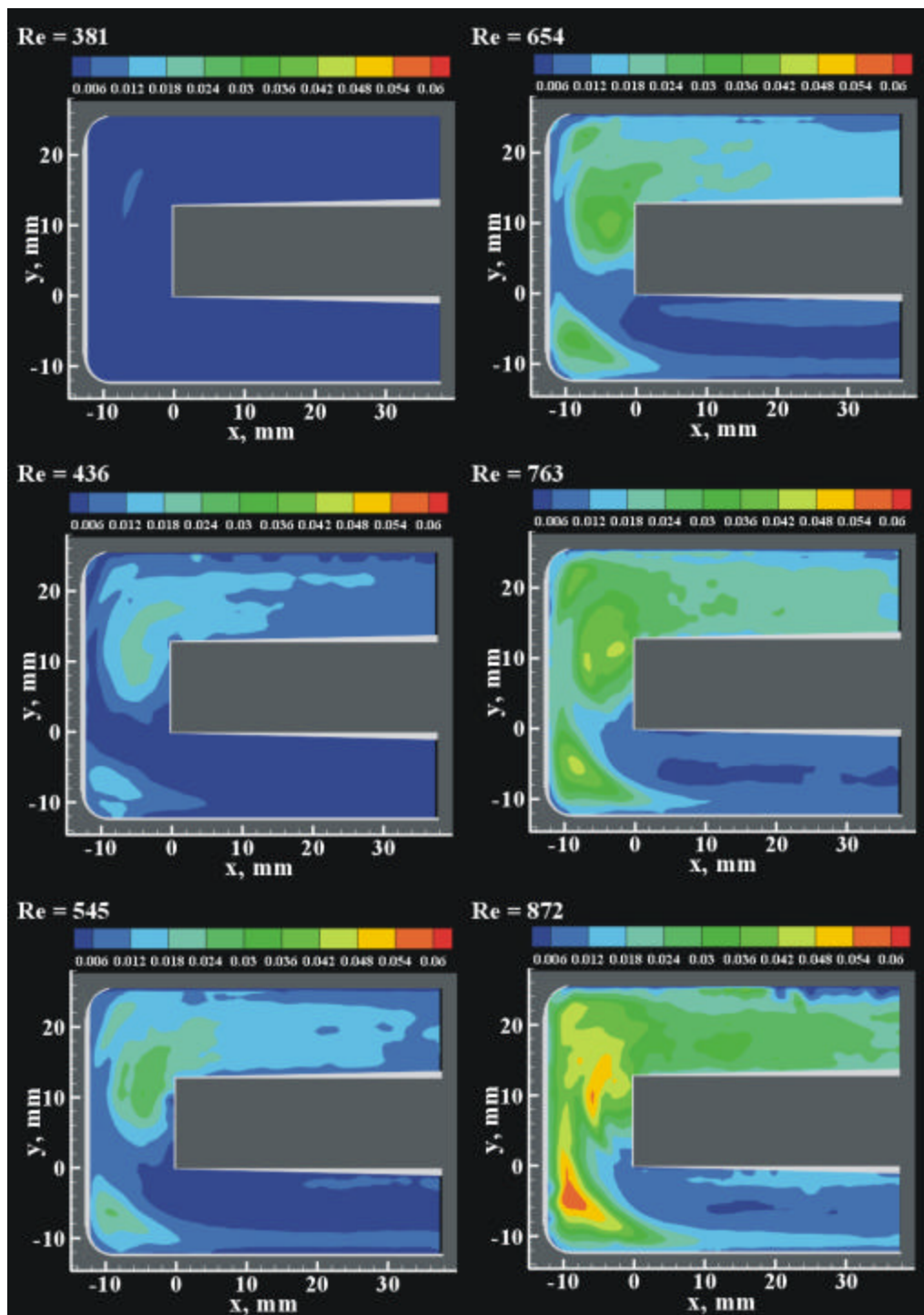
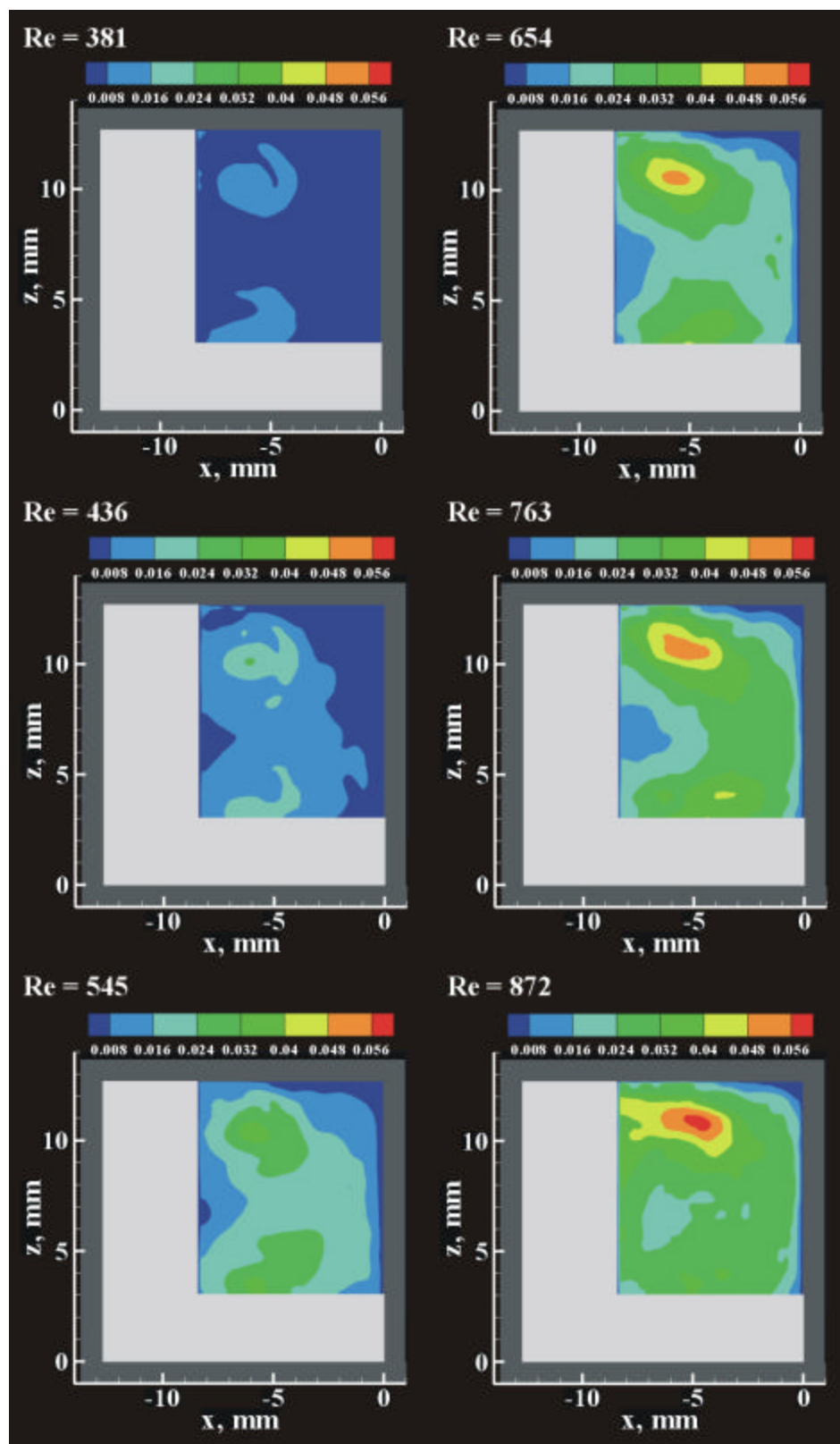**Figure 3.9:** RMS of the flow field in the primary flow plane for various Reynolds numbers.

Figure 3.10: RMS of the flow field in the secondary flow plane for various Reynolds numbers.

3.3.2 Reynolds Stress

The Reynolds stress patterns are presented in Figure 3.11, and show the same general trend with respect to increasing Reynolds number as the patterns of root-mean-square velocity fluctuations $|\underline{V}|_{rms}$ (Figure 3.9). The dominant flow structures that contribute to the largest values of $<u'v'>$ are the recirculation cells in the outer corners of the U-bend and the separated flow zone originating from the first (downstream) inner corner. In addition, at Re = 763 and Re = 872, elevated levels of $<u'v'>$ in the channel downstream of the U-bend indicate the increase in the background turbulence levels in this region.

Figure 3.12 shows patterns of Reynolds stress correlation $<u'w'>$ in the secondary flow plane. Each of the counter-rotating Dean vortices corresponds to two adjacent regions of elevated $<u'w'>$ of opposite sign. In fact, the magnitudes of $<u'w'>$ associated with the intermittent smaller-scale vortices that are present at higher Reynolds numbers are small in comparison with the organized $<u'w'>$ corresponding to the Dean vortices. This finding again emphasizes the dominant role of the natural instability of the Dean vortex structure over the background turbulence in the secondary flow plane.
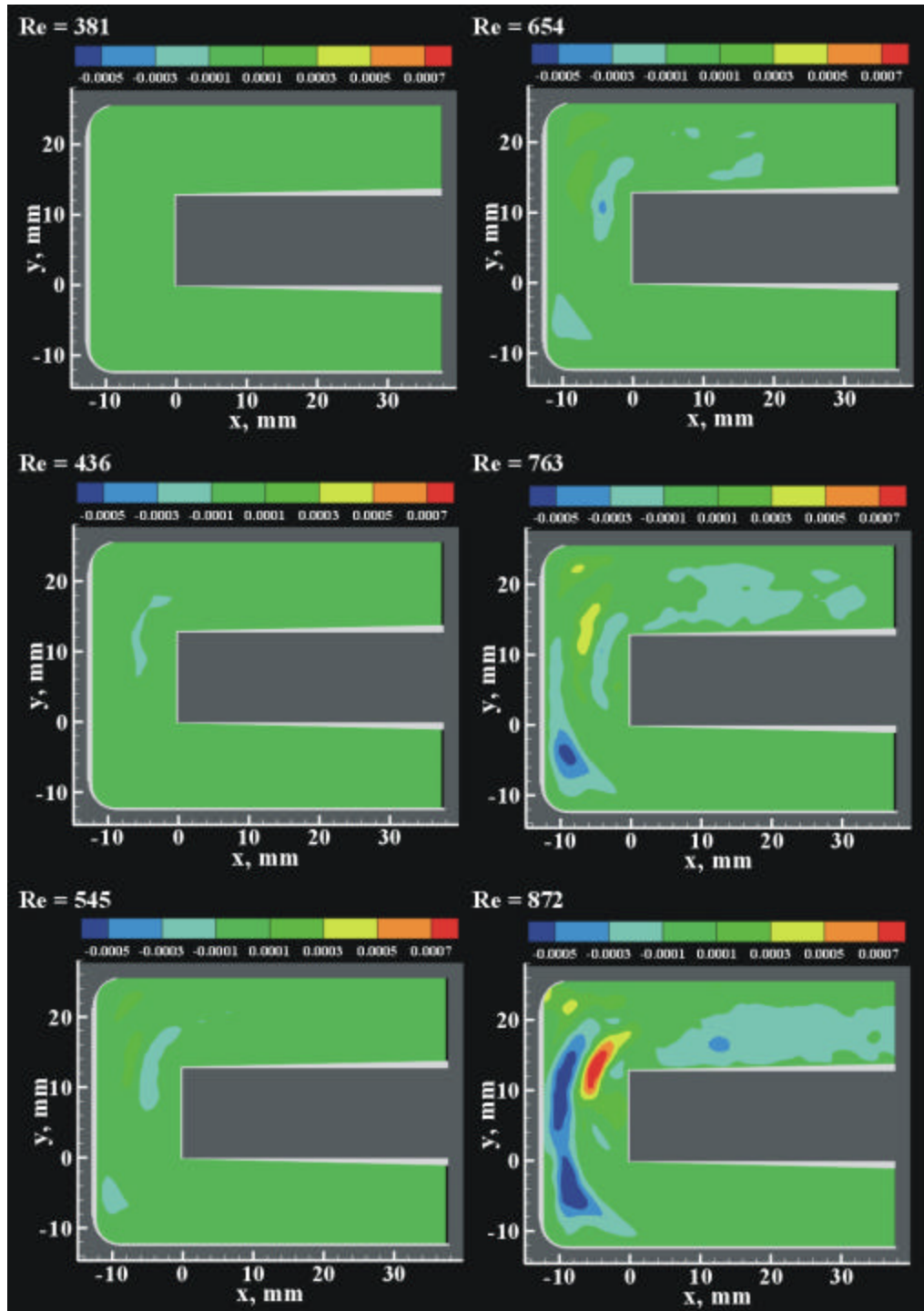
Figure 3.11: Reynolds stress of the flow field in the primary flow plane
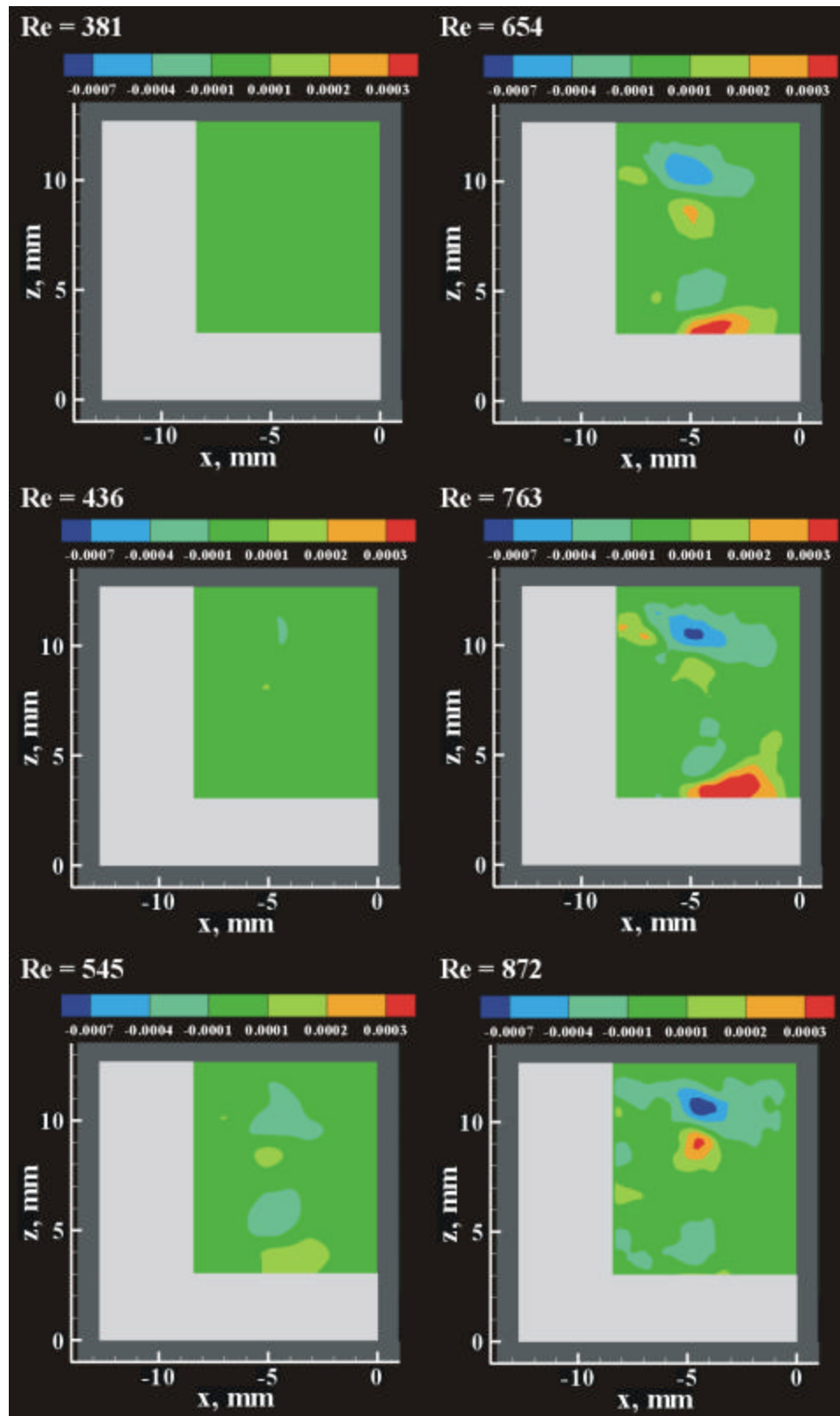for various Reynolds numbers.

Figure 3.12: Reynolds stress of the flow field in the secondary flow plane for various Reynolds numbers.

3.3.3 Oscillation Analysis

While the oscillatory characteristics of the flow are quite evident, it is unclear whether these oscillations occur at a constant or dominant frequency. Unfortunately the acquisition rate of the PIV system was insufficient to resolve the frequency of the oscillations. An approximate approach for estimating the oscillation frequency was therefore devised.

In the velocity streamline plots, as seen in Figure 3.4(a), some of the streamlines downstream from the U-bend have a periodic nature. It is inferred that these streamlines are the downstream manifestation of the oscillatory flow at the turn. Thus, the wavelength of the streamlines can be used to estimate the oscillation frequency of the separated flow at the first edge of the U-bend. Estimating the frequency of the oscillations is accomplished with Equation 10.

$$f \approx \frac{U_o}{\lambda} \tag{10}$$

Where f is the oscillation frequency of the shear layer, U_o is the velocity of the fluid in the oscillating shear layer, and λ is the wavelength of the oscillation.

The only additional information required was the velocity of the fluid in the shear layer at each of the Reynolds numbers. Velocity of the fluid in the shear layer was difficult to measure since the oscillations found in the streamlines of a particular image corresponded to oscillations at an unknown previous image. For each flow rate an estimated U_o was used, calculated as half the averaged centerline velocity of the fluid in the entrance channel. The shear layer velocity used at each Reynolds number was the same for all estimations of the oscillation frequency. Since the ability to determine the frequency estimate depended on finding a suitable velocity streamline plot, only 9-12

adequate images were found at each Reynolds number. Figure 3.13 contains the averaged frequency at each Reynolds number after the transition.
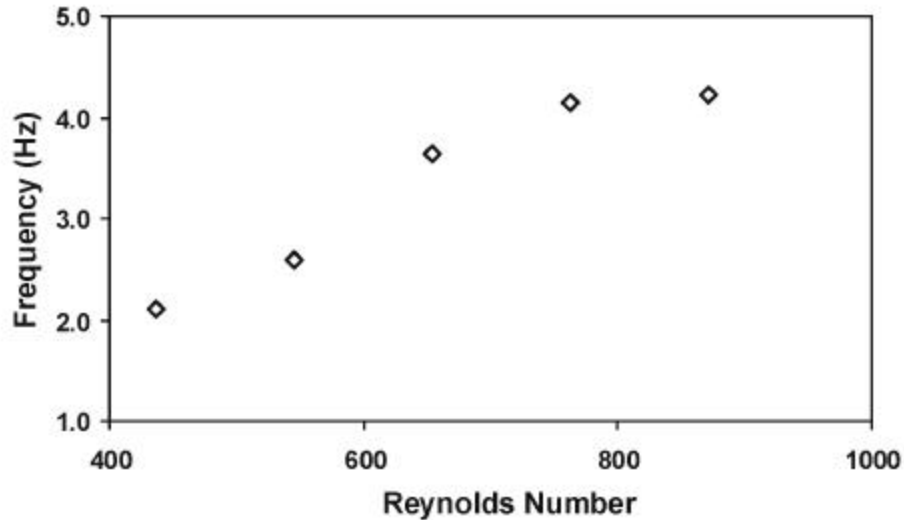

Figure 3.13: Estimation of the oscillation frequency of the flow separation at the first corner of the U-bend.

Although there are fewer points than are required to make definitive statements about the nature of the flow and despite the calculated frequency being merely an estimate, general trends can be observed. As would be expected, the frequency of the oscillations increases with increasing Reynolds number. However, it does appear that the frequency increases with Reynolds number at a less than linear rate.

3.4 Flow Relationships

To obtain a detailed understanding of the flow in a sharp U-bend requires more than an investigation of the flow in the various planes; it requires an understanding of the relationships between the flows in the various planes. Additionally, it is desirable to have a quantitative understanding of the changes in the flow rather than only a qualitative

understanding. To obtain further understanding of the flow, relationships involving the velocity, vorticity, RMS, and Reynolds stress were investigated.

3.4.1 Velocity Comparison

It was clear that the transition had an affect on the features of the flow at the various Reynolds numbers. To further investigate possible relationships, ratios of flow properties between the two planes were examined. One of the ratios examined was the velocity. Equation 11 describes the process used in examining both the maximum velocity and the average velocity.

$$\text{velocity ratio} ? \; \frac{U_s}{U_p} ? 100\% \tag{11}$$

Where U_s is the secondary velocity examined (maximum or average) and U_p is the primary velocity examined (maximum or average). The velocity examined is either the maximum velocity seen in the plane of interest or the average velocity seen in the plane of interest. Figure 3.14 contains the results for the entire range of Reynolds numbers.

It is clear that the ratio of the secondary velocity to primary velocity increases almost linearly for both the maximum and average velocities prior to the transition. Near the transition in the flow, the ratio reaches its maximum (approximately 98% for the maximum and 43% for the average). After the transition, the ratio decreases almost linearly. This implies that the relative secondary motion is at its highest near the transition. If one wants to maximize the secondary motion for a particular case, it would be desirable to operate as near the flow transition as possible.
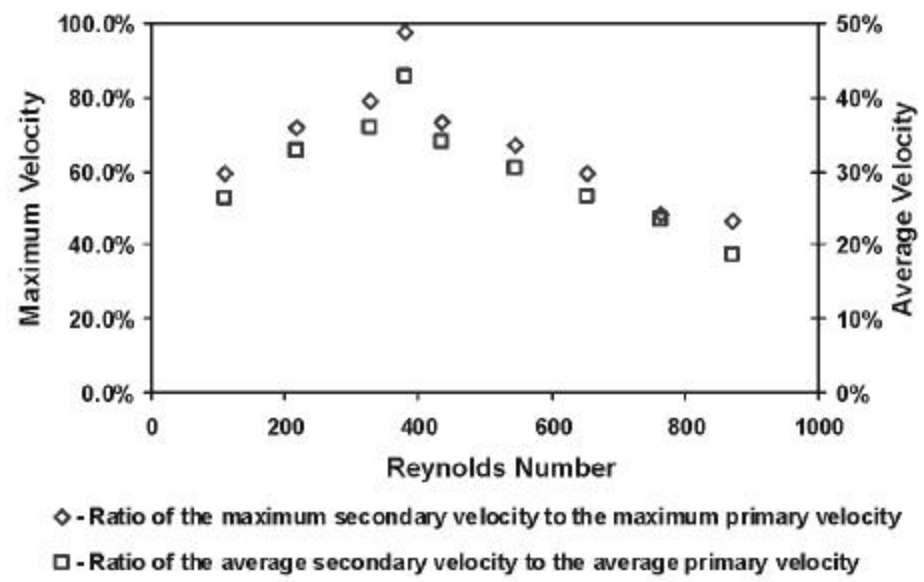
Figure 3.14: Ratio of the secondary velocity to the primary velocity.

3.4.2 Vorticity Comparison

As with the velocity, a vorticity ratio was examined. The major difference between the approaches taken for the two properties was that rather than looking at the maximum and averaged values, for vorticity the maximum positive and maximum negative values were examined.

A general equation is shown in Equation 12, which describes the manner in which both ratios are calculated.

$$\text{maximum vorticity ratio } ? \ \frac{\max\{?_y\}}{\max\{?_z\}}?100\% \tag{12}$$

The results, shown in Figure 3.15, demonstrate a trend in the negative vorticity similar to that for the velocity. Prior to the transition, the negative vorticity ratio increases almost linearly to a maximum at the transition. After the transition, the ratio

decreases almost linearly with increasing Reynolds number. The positive vorticity, however, does not show as clear a trend. While the ratio does reach a maximum at the transition, there is only a general increase and decrease in the ratio, prior to and after the transition, respectively. It is unclear whether this feature of the positive vorticity is a true feature of the flow field or an effect of the optically inaccessible regions in the secondary flow plane.
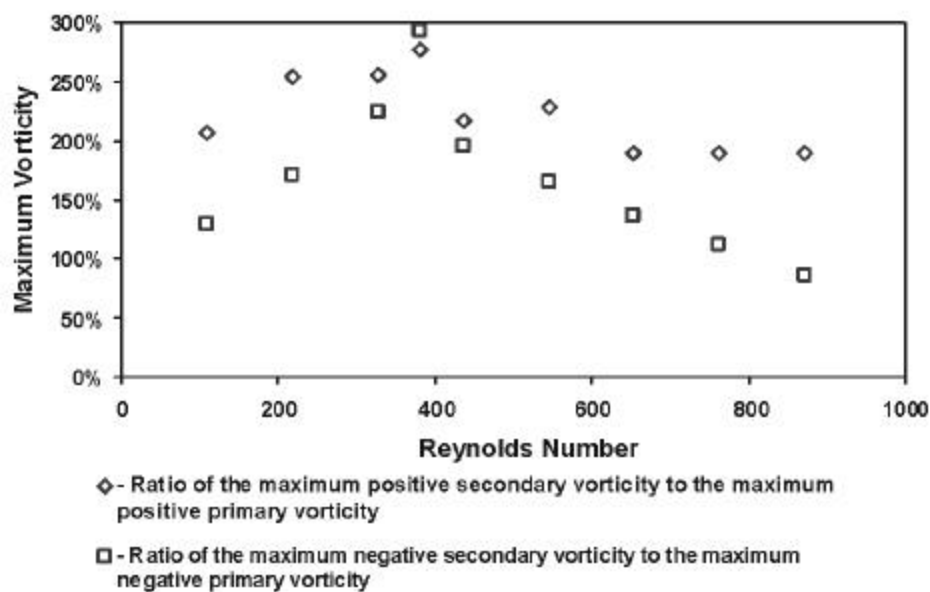

◇ - Ratio of the maximum positive secondary vorticity to the maximum positive primary vorticity

□ - Ratio of the maximum negative secondary vorticity to the maximum negative primary vorticity

Figure 3.15: Ratio of the secondary vorticity to the primary vorticity. The positive direction refers counterclockwise rotation, while the negative direction refers to clockwise rotation.

3.4.3   RMS Comparison

The RMS was investigated in a similar manner to the velocity and vorticity. Since the RMS is only a relevant quantity after the transition, only the post-transition data could be examined. Unlike the velocity and vorticity data, the RMS ratio showed no distinct trend with increasing Reynolds number.

An additional approach was used in which a normalized RMS was examined for each view of the post-transition Reynolds numbers. While this approach failed to give any clear results, it is mentioned because the same approach was used for the Reynolds stress with better results.

3.4.4 Reynolds Stress Comparison

As with the RMS data, a ratio in the Reynolds stress was only applicable after the transition and showed no clear trend. Unlike the RMS data, however, a normalized Reynolds stress examination was a beneficial analysis. The normalized Reynolds stress was calculated according to Equation 13 and 14.

$$norm \; u'v' = \frac{\langle u'v' \rangle}{U_b} \tag{13}$$

$$norm \; u'w' = \frac{\langle u'w' \rangle}{U_b} \tag{14}$$

Where $norm \; u'v'$ is the normalized Reynolds stress in the primary plane, $norm \; u'w'$ is the normalized Reynolds stress in the secondary plane and U_b is the bulk velocity in the primary plane based on the flowrate. Figure 3.16 and Figure 3.17 contain the normalized Reynolds stress results for the post-transition Reynolds number in the primary and secondary flow planes respectively.
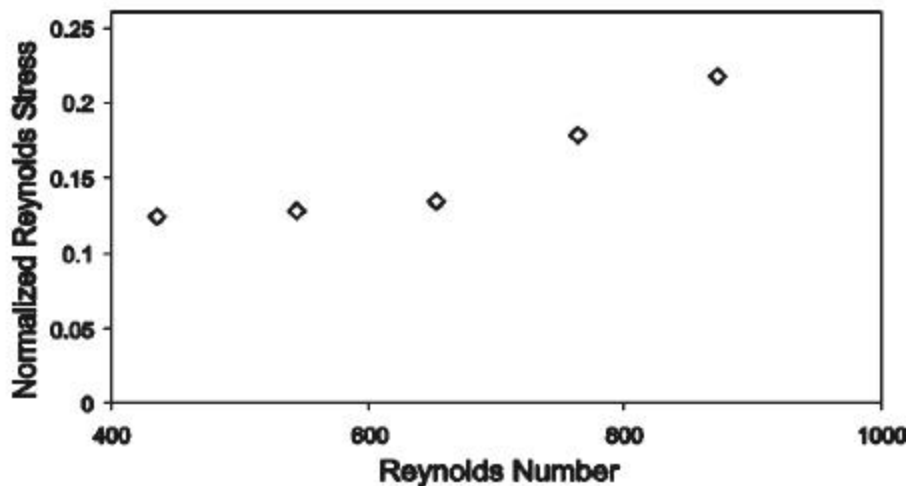
Figure 3.16: Normalized Reynolds stress for the primary flow plane at various post-transition Reynolds numbers.
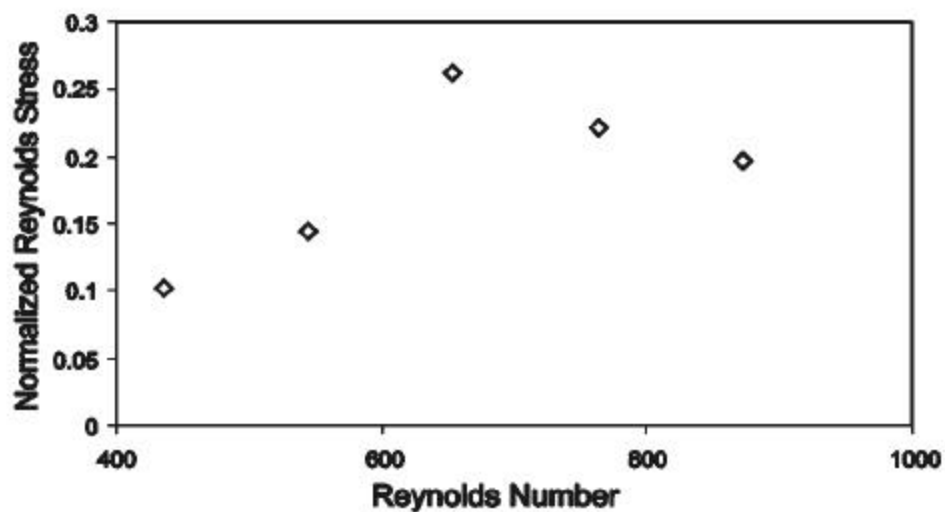

Figure 3.17: Normalized Reynolds stress for the secondary flow plane at various post-transition Reynolds numbers.

An interesting phenomena is that while the normalized Reynolds stress in the primary flow plane demonstrates an exponential like increase for the Reynolds numbers observed, the normalized Reynolds stress in the secondary flow plane does not show a trend with increasing Reynolds number. It is implied that while the turbulent mixing

develops differently in the secondary plane than in the primary plane. Similar to the phenomena observed in the velocity and vorticity comparisons, high Re flow may not be the most effective way to achieve proper mixing.

3.5   *Implications for Numerical Modeling*

Recently, computational fluid dynamics (CFD) techniques have gained popularity for modeling the reactions within fuel cells. Several research groups have investigated the use of CFD for fuel cells including Nguyen *et al.* [1] at the University of Victoria, Siegel *et al.* [2] at Virginia Polytechnic and State University, Kumar and Reddy [3] at the University of Alabama and Wang *et al.* [4] at the University of Miami. Varying aspects of fuel cells have been examined by each of the groups utilizing different approaches. Nguyen *et al.* produced a comprehensive three-dimensional model accounting for the major transport phenomena in a PEM fuel cell. Siegel *et al.* also accounted for the major transport phenomena, but focused primarily on the catalyst geometry through the implementation of a two-dimensional model. Kumar and Reddy used a three-dimensional half-cell model to examine the effects of channel dimension and shape on the performance of a PEM fuel cell. Wang *et al.* compared their experimental results with a comprehensive three-dimensional model coupling performance with chemical reaction kinetics.

Despite the differences between the approaches and focus of each of these research groups each of them assumed a stable laminar flow profile. As shown in this study, this assumption is false at all but the lowest Reynolds numbers commonly observed in a fuel cell. If accurate modeling of fuel cell behavior is desired, it is necessary to include the instabilities in both the primary and secondary flow planes.

Inclusion of the instabilities in the secondary flow plane is the most crucial since they are directly related to mixing and show a drastic breakdown of the two-vortex Dean type flow seen in stable flow.

CHAPTER 4   CONCLUSIONS

Through the application of Particle Imaging Velocimetry (PIV), a detailed investigation of the flow characteristics in a section of a serpentine flow channel was acquired. The 180 degree U-bend, utilized to simulate the first two passes of a serpentine channel, provided information on the onset of instability in laminar flow at increasing Reynolds numbers as well as primary and secondary flow characterizations. The flow information was characterized in terms of the instantaneous and time-averaged representations of the velocity vector field, out-of-plane vorticity contours, and vector streamlines.

At Re = 381, the flow in the bend was time independent and was stable downstream from the bend. The time independent nature of the flow in the bend was seen in both the primary and secondary flow planes. While flow separation occurred at the first edge of the U-bend it reattaches by the second edge. At Re = 436, however, the flow in the bend was clearly time dependent in both the primary and secondary flow planes. This unsteadiness was a result of the flow separation at the first edge no longer reattaching by the second edge.

Three unsteadiness parameters, RMS, Reynolds stress and the frequency of the oscillation, were used to characterize the flow after the transition. The RMS and Reynolds stress both increased with increasing Reynolds number. The oscillation frequency analysis showed that the frequency increases less than linearly with increasing Reynolds number.

Additionally, a quantitative analysis of the flow parameters was performed in two ways. For the velocity and vorticity, the ratio of the secondary plane flow measurements

to the primary plane flow measurements was examined. In general, there was a near linear increase in the ratio prior to the transition, where it reached a maximum and a near linear decrease in the ratio after the transition.

The ratio approach did not provide meaningful results for the RMS and Reynolds stress after the transition. However, examination of the normalized Reynolds stresses in the primary flow plane showed an exponential increase for the Reynolds numbers examined. In contrast, the normalized Reynolds stress does not show a general trend in the secondary flow plane. The normalization approach did not provide additional insight into the behavior of RMS velocities.

These various aspects of the flow explored in this thesis provide a better understanding of flow in a sharp U-bend at low Reynolds numbers. While this study in itself does not increase design capabilities for fuel cells, it does provide the basis to do so on two fronts. The first is to imply the benefits of detailed investigations into channels at smaller scales, a larger range of Reynolds numbers, or both. Secondly, the results clearly highlight the inadequacy of the steady laminar flow assumptions in certain flow regimes, and the need for parameterization of the flow in models coupling transport phenomena and electrochemistry. The data obtained in this thesis can be used to validate improved numerical models of fuel cells, and enhance the reliability of such models for design.

REFERENCES

[1] Nguyen, P. T., Berning, T., and Djilali, N., 2004, Computational model of a PEM fuel cell with serpentine gas flow channels, *Journal of Power Sources*, Vol. 130, pp. 149-157.

[2] Siegel, N. P., Ellis, M. W., Nelson, D. J., von Spakovsky, M. R., 2003, Single domain PEMFC model based on agglomerate catalyst geometry, *Journal of Power Sources*, Vol. 115, pp. 81-89.

[3] Kumar, A. and Reddy, R. G., 2003, Effect of channel dimensions and shape in the flow-field distributor on the performance of polymer electrolyte membrane fuel cells, *Journal of Power Sources*, Vol. 113, pp. 11-18.

[4] Wang, L., Husar, A., Zhou, T., and Liu, H., 2003, A parametric study of PEM fuel cell performances, *Int. J. Hydrogen Energy,* Vol. 28, pp. 1263-1272 .

[5] Dean, W. R., 1928, Fluid Motion in a Curved Channel, *Proceedings of the Royal Society of London A*, Vol. 121, pp. 402-420.

[6] Hawthorne, W. R., 1951, Secondary Circulation in Fluid Flow, *Proceedings of the Royal Society of London A*, Vol. 206, pp. 374-387.

[7] Agrawal, Y., Talbot, L., and Gong, K., 1978, Laser anemometer study of flow development in curved circular pipes, *J. Fluid Mechanics*, Vol. 85, pp. 497-518.

[8] Olson, D. E. and Snyder, B., 1985, The upstream scale of flow development in curved circular pipes, *Journal of Fluid Mechanics*, Vol. 150, pp. 139-158.

[9] Lin, J. Y. and Tarbell, J. M., 1980, An experimental and numerical study of periodic flow in a curved tube, *Journal of Fluid Mechanics*, Vol. 100, pp. 623-638.

[10] Berger, S. A. and Talbot, L., 1983, Flow in Curved Pipes, *Annual Review of Fluid Mechanics*, Vol. 15, pp. 461-512.

[11] Humphrey, J. A. C., Taylor A. M. K. and Whitelaw, J. H., 1977, Laminar flow in a square duct of strong curvature, *Journal of Fluid Mechanics*, Vol. 83, pp. 509-527.

[12] Bara, B., Nandakumar, K. and Masliyah, J. H., 1992, An experimental and numerical study of the Dean problem: flow development towards two-dimensional multiple solutions, *Journal of Fluid Mechanics*, Vol. 244, pp. 339-376.

[13] Mees, Philip A. J., Nandakumar, K. and Masliyah, J. H., 1996, Instability and transitions of flow in a curved square duct: the development of two pairs of Dean vortices, *Journal of Fluid Mechanics*, Vol. 314, pp. 227-246.

[14] Gauthier, G., Gondret, P., Thome, H., and Rabaud, M., 2001, Centrifugal instabilities in a curved rectangular duct of small aspect ratio, *Physics of Fluids*, Vol. 13, pp. 2831-2834.

[15] Chintada, S., Ko, K. H. and Anand, N. K., 1999, Heat transfer in 3-D serpentine channels with right-angle turns, *Numerical Heat Transfer A*, Vol. 36, pp. 781-806.

[16] Mochizuki, S., Murata, A., Shibata, R. and Yang, W. J., 1999, Detailed measurements of local heat transfer coefficients in turbulent flow through smooth and rib roughened serpentine passages with a 180 degrees sharp bend, *International Journal of Heat and Mass Transfer*, Vol. 42, pp. 1925-1934.

[17] Choi, J. M. and Anand, N. K., 1993, Heat-Transfer in a Serpentine Channel with a Series of Right-Angle Turns, *Numerical Heat Transfer A*, Vol. 23, pp. 189-210.

[18] Adrian, R.J., 1991, Particle-Imaging Techniques for Experimental Fluid Mechanics, *Annual Review of Fluid Mechanics*, Vol. 23, pp. 261-304.

[19] LaVision GmbH. *FlowMaster Manual*. Germany: LaVision, 2002.

[20] Westerweel, J., 1997, Fundamentals of digital particle image velocimetry, *Measurement Science & Technology*, Vol. 8, pp. 1379-1392.

[21] Olsen, M. G. and Adrian, R. J., 2000, Brownian motion and correlation in particle image velocimetry, *Optics and Laser Technology*, Vol. 32, pp. 621-627.

[22] Guezennec, Y. G. and Kiritsis, N., 1990, Statistical Investigation of Errors In Particle Image Velocimetry, *Experiments in Fluids*, Vol. 10, pp. 138-146.

[23] Huang, H. T., Fiedler, H. E. and Wang, J. J., 1993, Limitation and Improvement of PIV: 1. Limitation of Conventional Techniques Due to Deformation of Particle Image Patterns, *Experiments in Fluids*, Vol. 15, pp. 168-174.

[24] Huang, H. T., Fiedler, H. E. and Wang, J. J., 1993, Limitation and Improvement of PIV: 2. Particle Image Distortion, a Novel Technique, Experiments in Fluids, Vol. 15, pp. 263-273.

[25] Meinhart, C. D., Wereley, S. T. and Santiago, J. G., 2000, A PIV algorithm for estimating time-averaged velocity fields, *Journal of Fluids Engineering*, Vol. 122, pp. 285-289.

[26] Wereley, S. T. and Meinhart, C. D., 2001, Second-order accurate particle image velocimetry, *Experiments in Fluids*, Vol. 31, pp. 258-268.

[27] Hart, D. P., 2000, PIV error correction, *Experiments in Fluids*, Vol. 29, pp. 13-22.

[28] Huang, H., Dabiri, D. and Gharib, M., 1997, On errors of digital particle image velocimetry, *Measurement Science & Technology*, Vol. 8, pp. 1427-1440.

[29] Gui, L. and Merzkirch, W., 2000, A comparative study of the MDQ method and several correlation-based PIV evaluation algorithms, *Experiments in Fluids*, Vol. 28, pp. 36-44.

[30] Westerweel, J., Dabiri, D. and Gharib, M., 1997, The effect of a discrete window offset on the accuracy of cross-correlation analysis of digital PIV recordings, *Experiments in Fluids*, Vol. 23, pp. 20-28.

[31] Scarano, F. and Riethmuller, M. L., 1999, Iterative multigrid approach in PIV image processing with discrete window offset, *Experiments in Fluids*, Vol. 26, pp. 513-523.

[32] Forliti, D. J., Strykowski, P. J. and Debatin, K., 2000, Bias and precision errors of digital particle image velocimetry, *Experiments in Fluids*, Vol. 28, pp. 436-447.

[33] Willert, C. E. and Gharib, M., 1991, Digital Particle Image Velocimetry, *Experiments in Fluids*, Vol. 10, pp. 181-193.

[34] Lourenco, L. and Krothapalli, A., 1995, On the Accuracy of Velocity and Vorticity Measurements With PIV, *Experiments in Fluids*, Vol. 18, pp. 421-428.

[35] Westerweel, J., 2000, Theoretical analysis of the measurement precision in particle image velocimetry, *Experiments in Fluids*, Vol 29, pp. S3-S12.

[36] Nogueira, J., Lecuona, A. and Rodriguez, P. A., 1997, Data validation, false vectors correction and derived magnitudes calculation on PIV data, *Measurement Science & Technology*, Vol. 8, pp. 1493-1501.

[37] Ruan, X., Song, X. and Yamamoto, F., 2001, Direct measurement of the vorticity field in digital particle images, *Experiments in Fluids*, Vol. 30, pp. 696-704.

[38] Abrahamson, S. and Lonnes, S., 1995, Uncertainty in Calculating Vorticity from 2D Velocity-Fields Using Circulation and Least-Squares Approaches, *Experiments in Fluids*, Vol. 20, pp. 10-20.
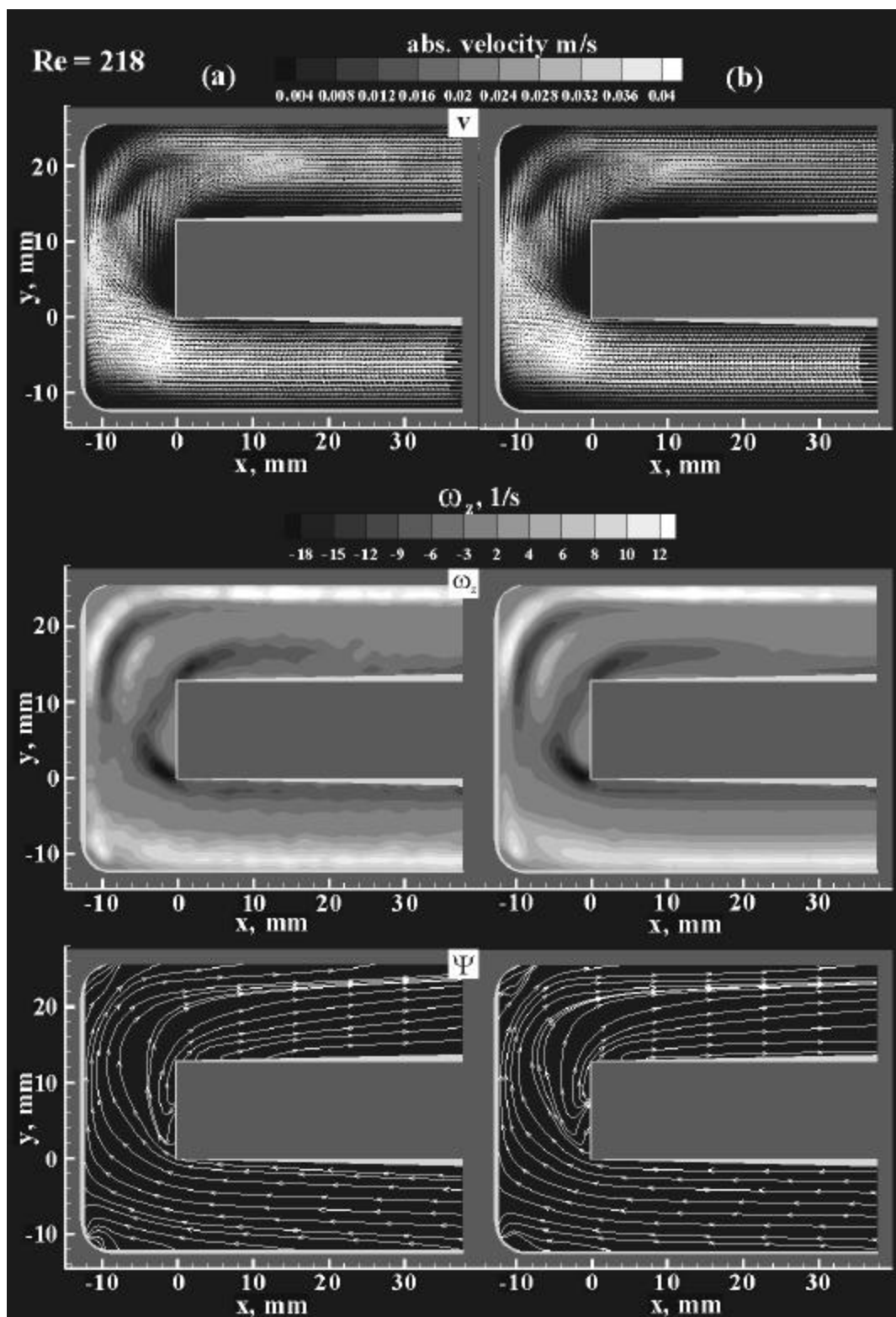
APPENDIX A: PRIMARY FLOW PLANE VISUALIZATIONS

Figure A.1: (a) Instantaneous and (b) averaged flow fields for the primary flow plane at Re = 218. From top to bottom: velocity vector field; out-of-plane vorticity contours; velocity streamlines.
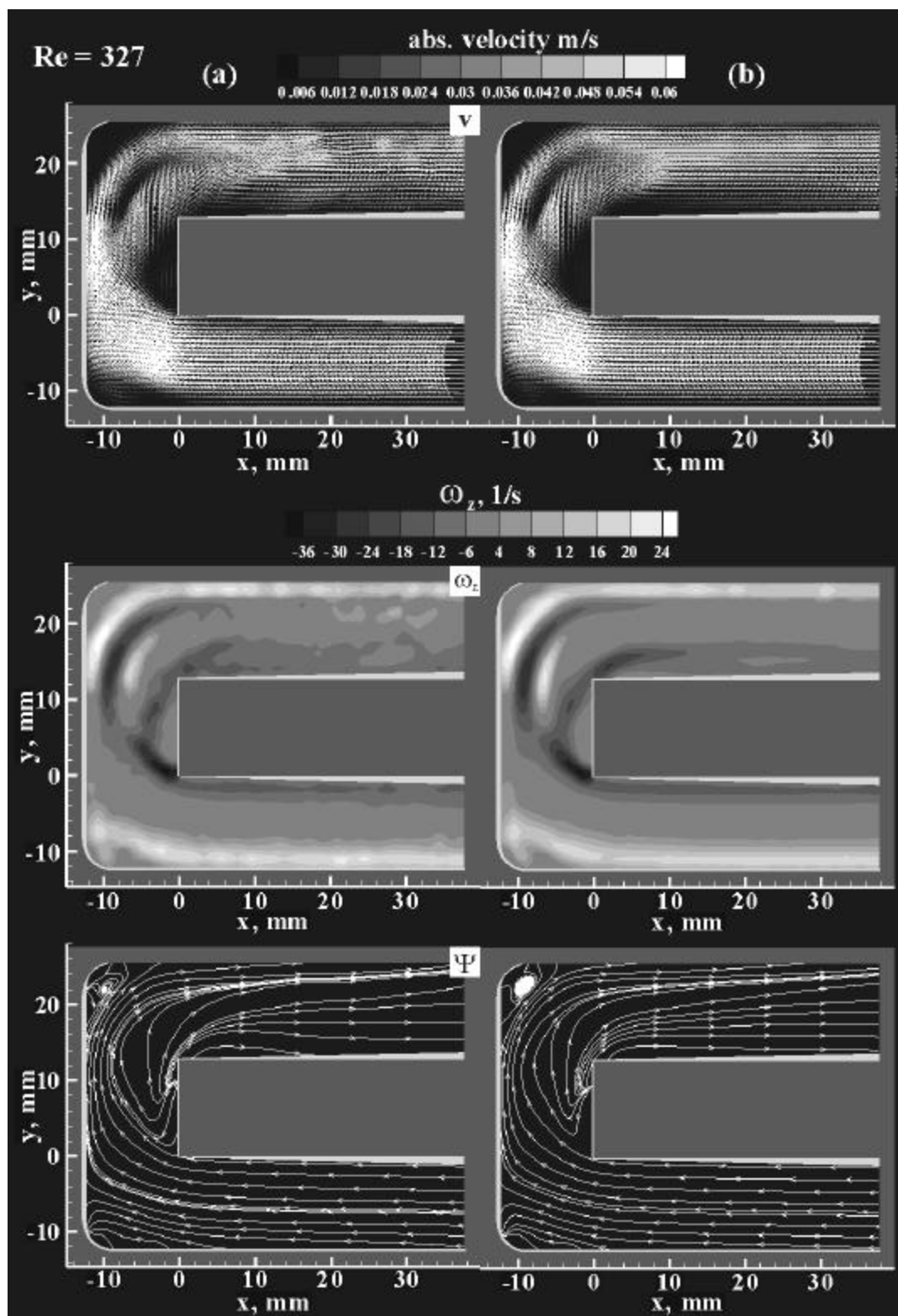
Figure A.2: (a) Instantaneous and (b) averaged flow fields for the primary flow plane at Re = 327. From top to bottom: velocity vector field; out-of-plane vorticity contours; velocity streamlines.
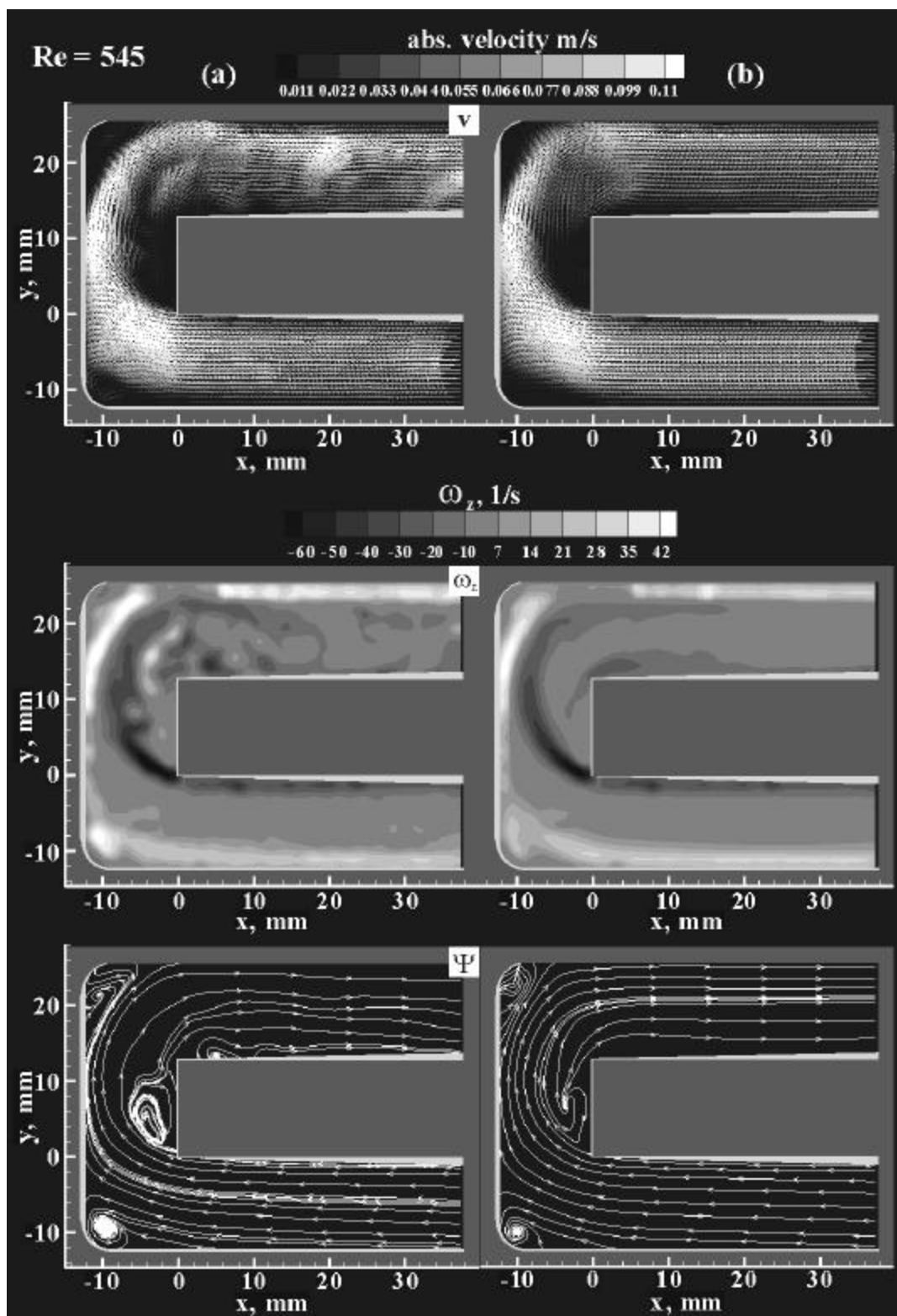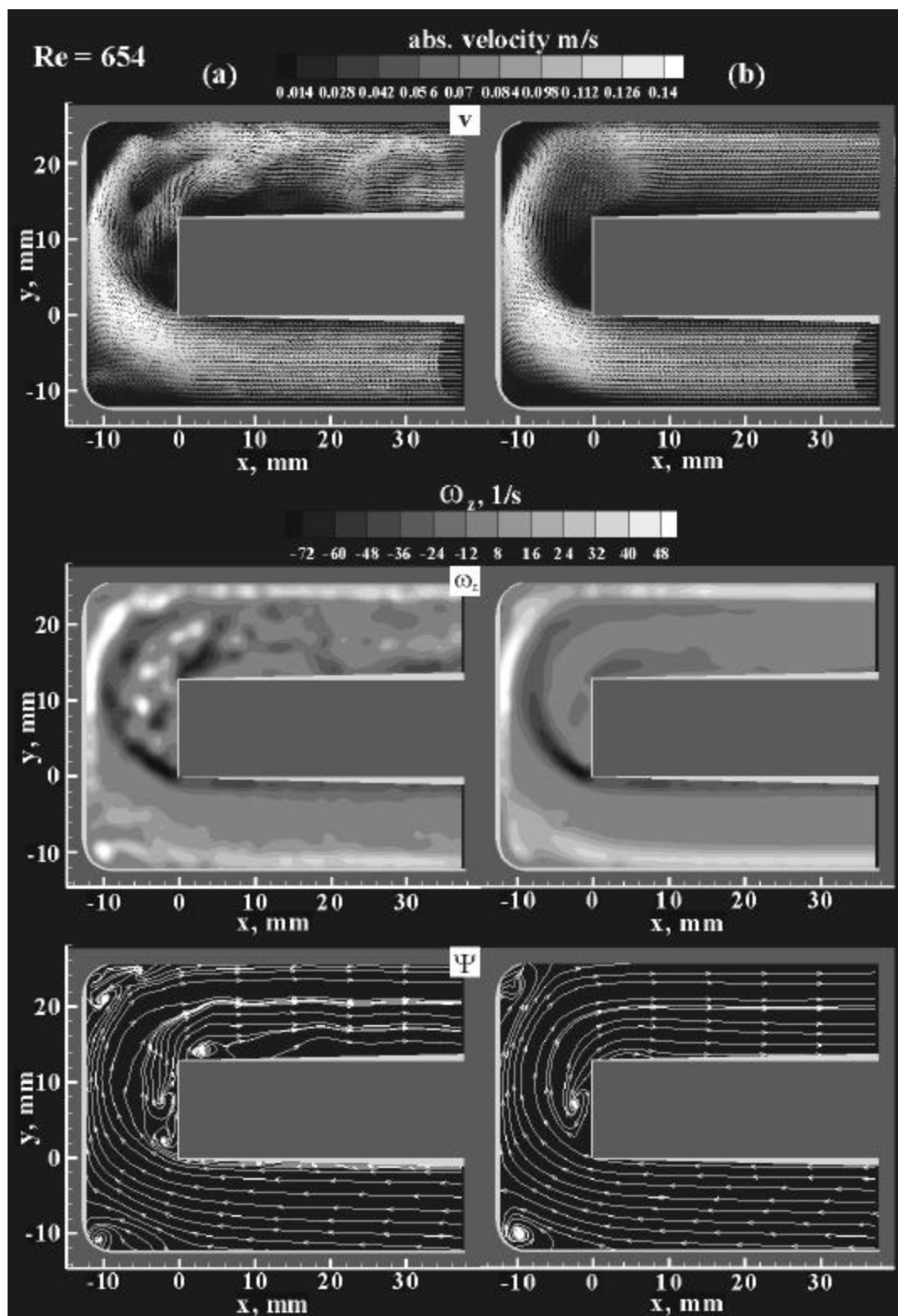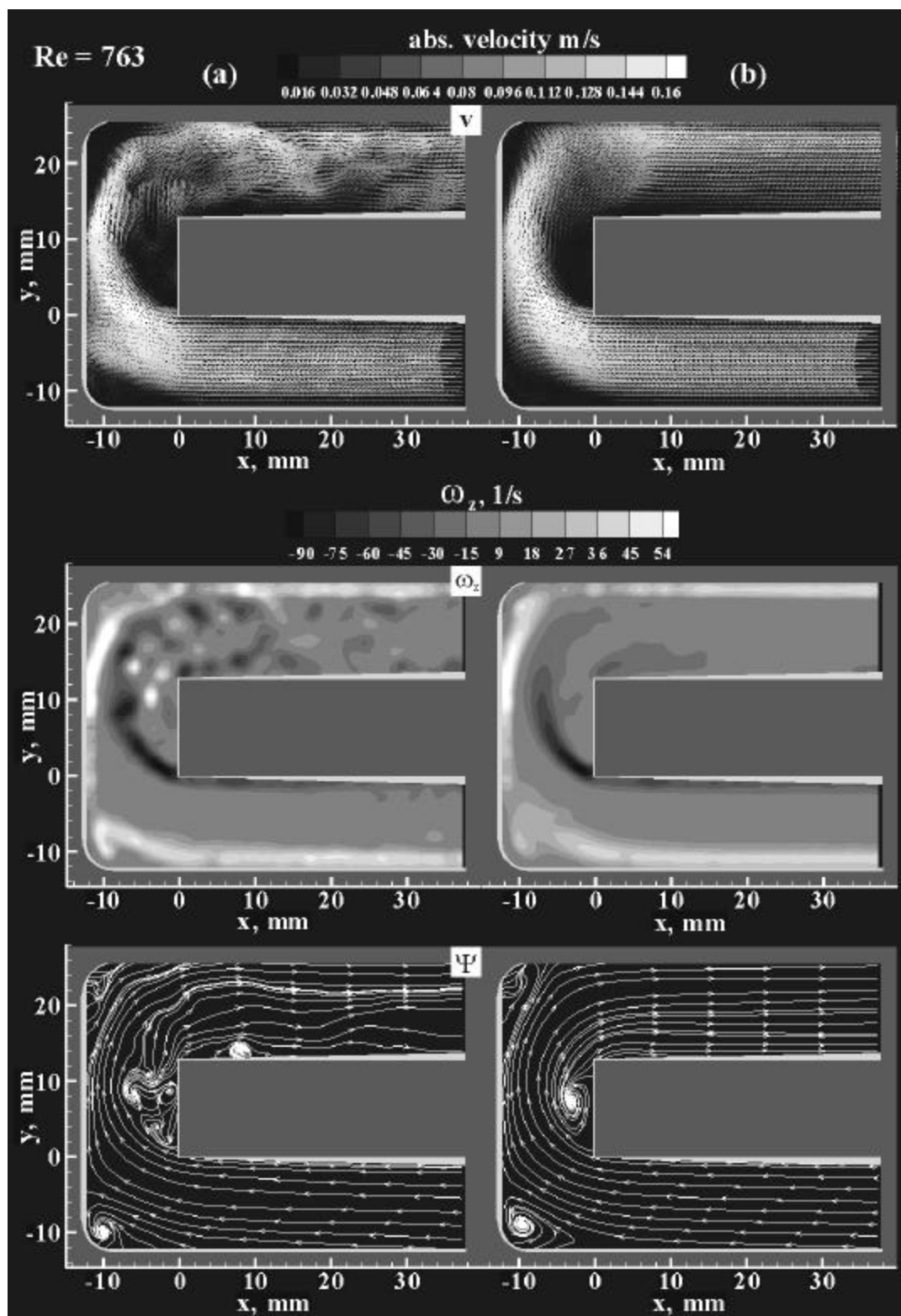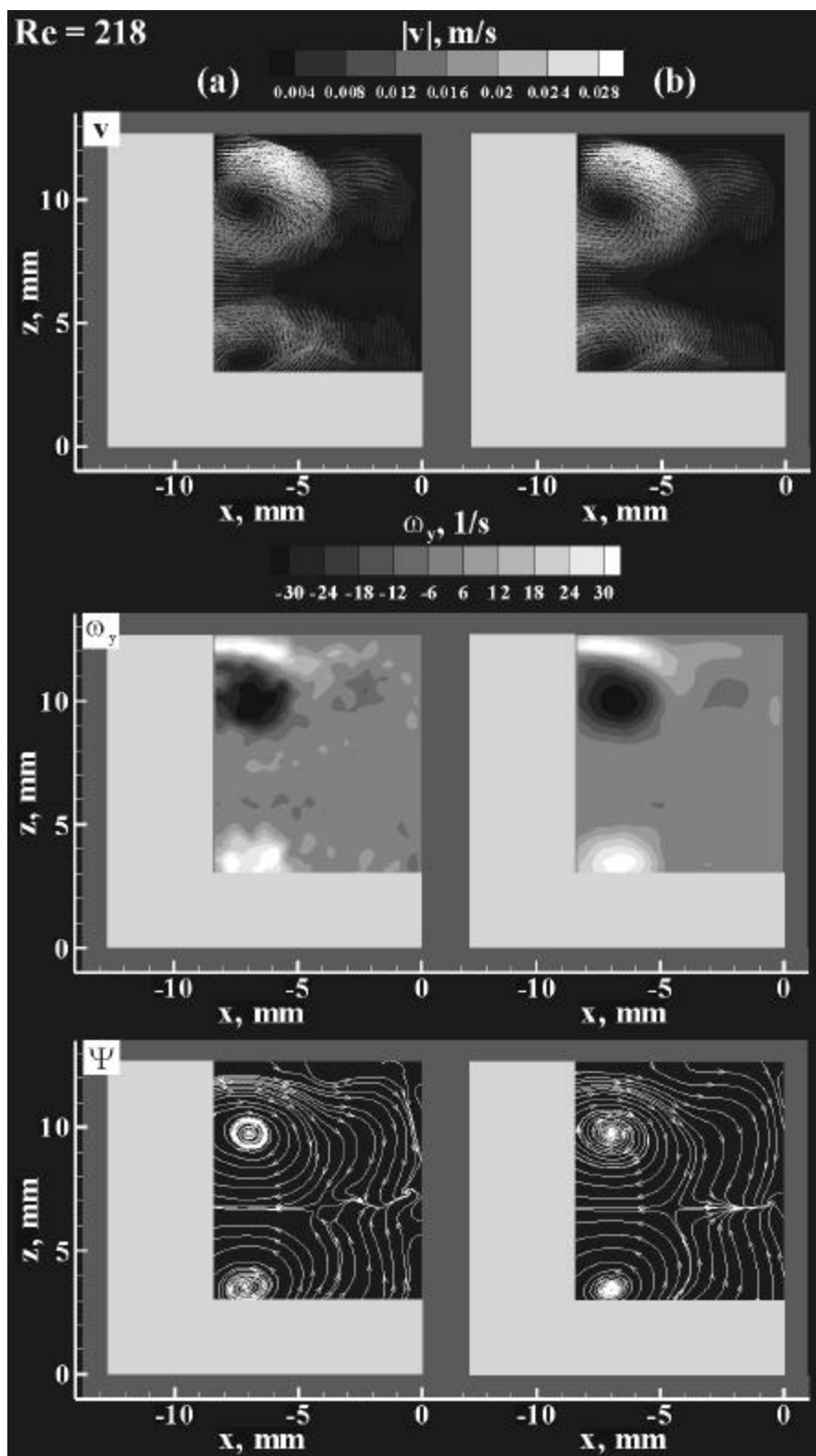
Figure A.3: (a) Instantaneous and (b) averaged flow fields for the primary flow plane at Re = 545. From top to bottom: velocity vector field; out-of-plane vorticity contours; velocity streamlines.

Figure A.4: (a) Instantaneous and (b) averaged flow fields for the primary flow plane at Re = 654. From top to bottom: velocity vector field; out-of-plane vorticity contours; velocity streamlines.

Figure A.5: (a) Instantaneous and (b) averaged flow fields for the primary flow plane at Re = 763. From top to bottom: velocity vector field; out-of-plane vorticity contours; velocity streamlines.

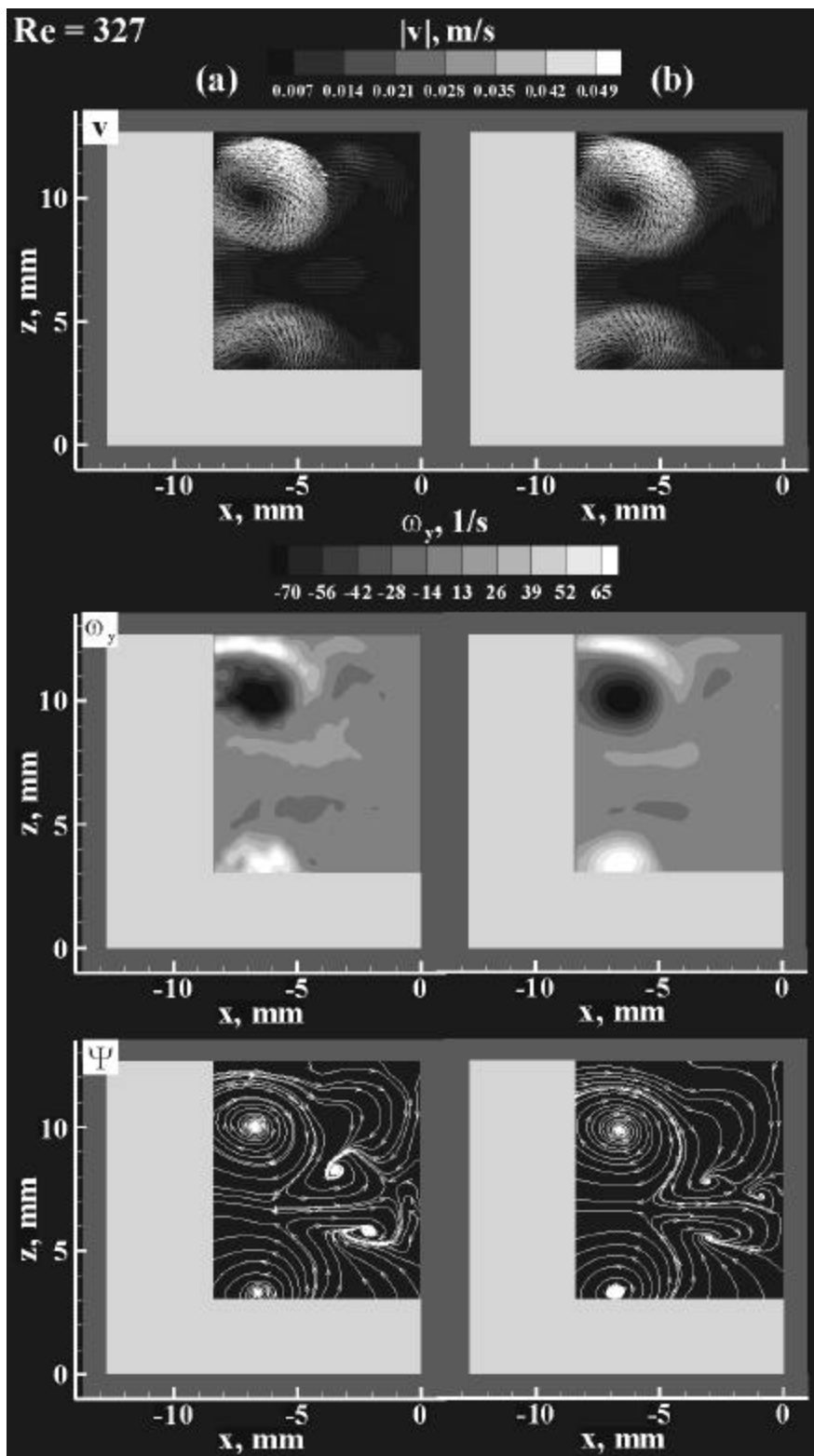# APPENDIX B: SECONDARY FLOW PLANE VISUALIZATIONS

Figure B.1: (a) Instantaneous and (b) averaged flow fields for the secondary flow plane at Re = 218. From top to bottom: velocity vector field; out-of-plane vorticity contours; velocity streamlines.
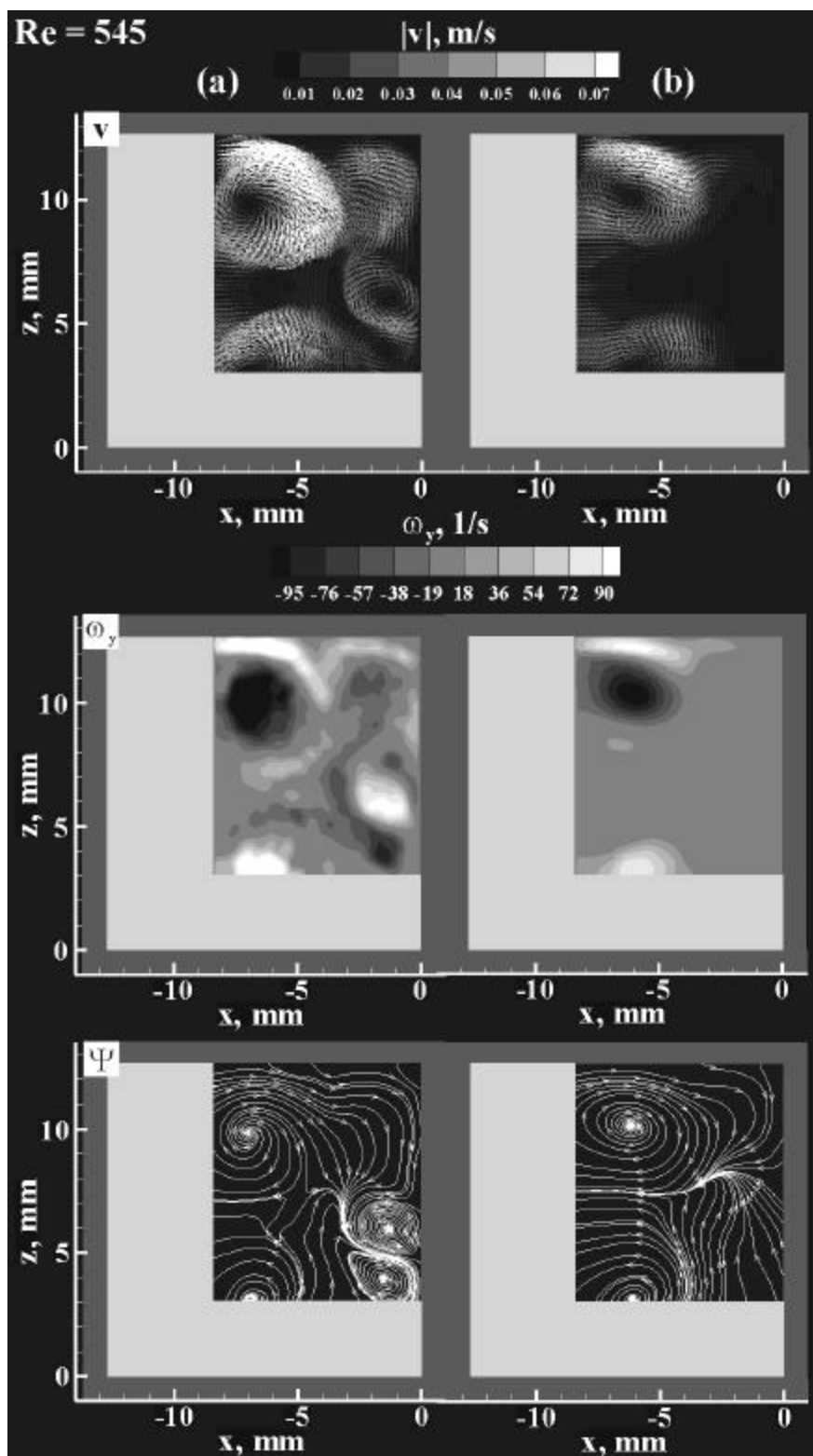
Figure B.2: (a) Instantaneous and (b) averaged flow fields for the secondary flow plane at Re = 327. From top to bottom: velocity vector field; out-of-plane vorticity contours; velocity streamlines.

Figure B.3: (a) Instantaneous and (b) averaged flow fields for the secondary flow plane at Re = 545. From top to bottom: velocity vector field; out-of-plane vorticity contours; velocity streamlines.
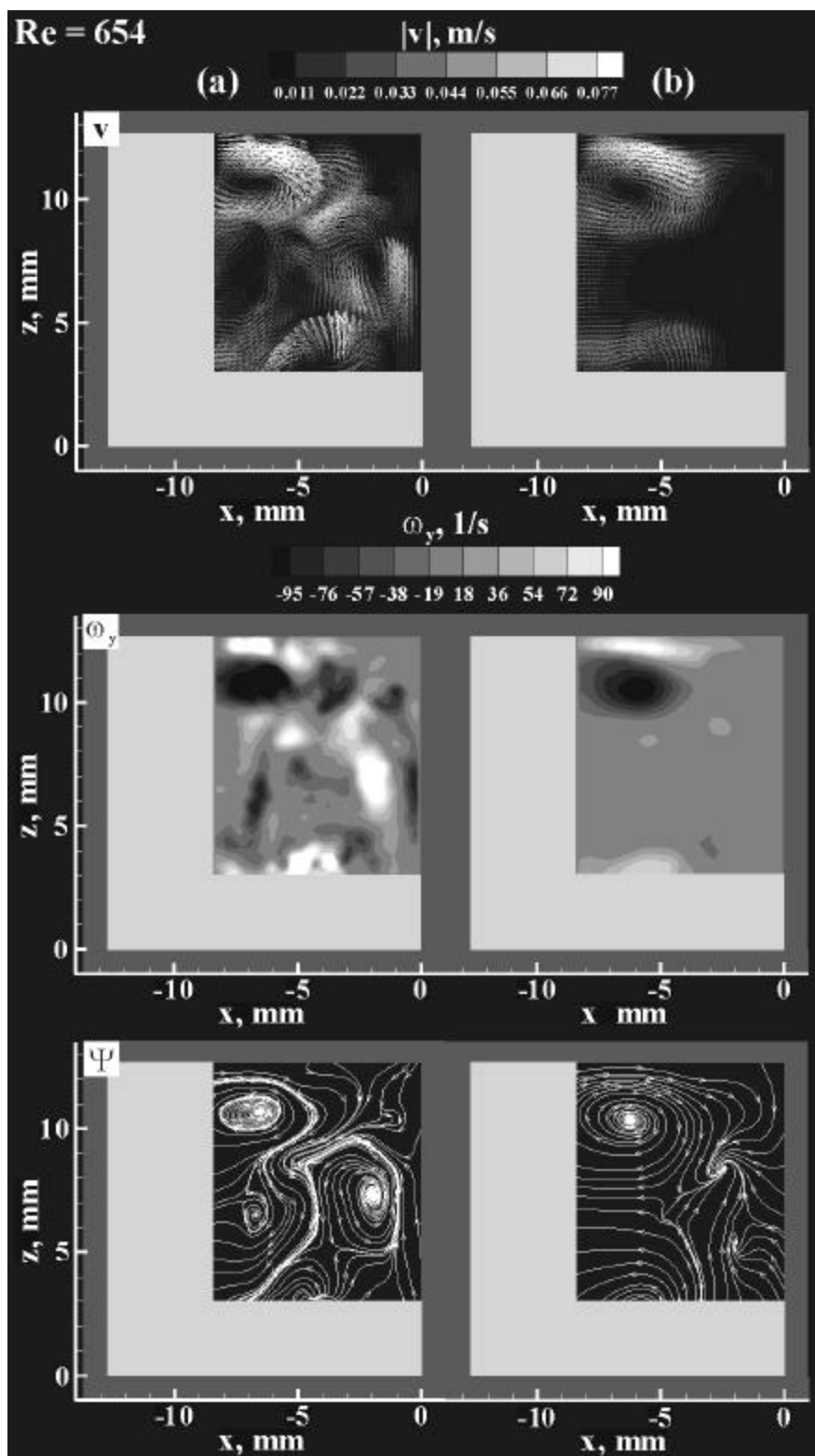
Figure B.4: (a) Instantaneous and (b) averaged flow fields for the secondary flow plane at Re = 654. From top to bottom: velocity vector field; out-of-plane vorticity contours; velocity streamlines.
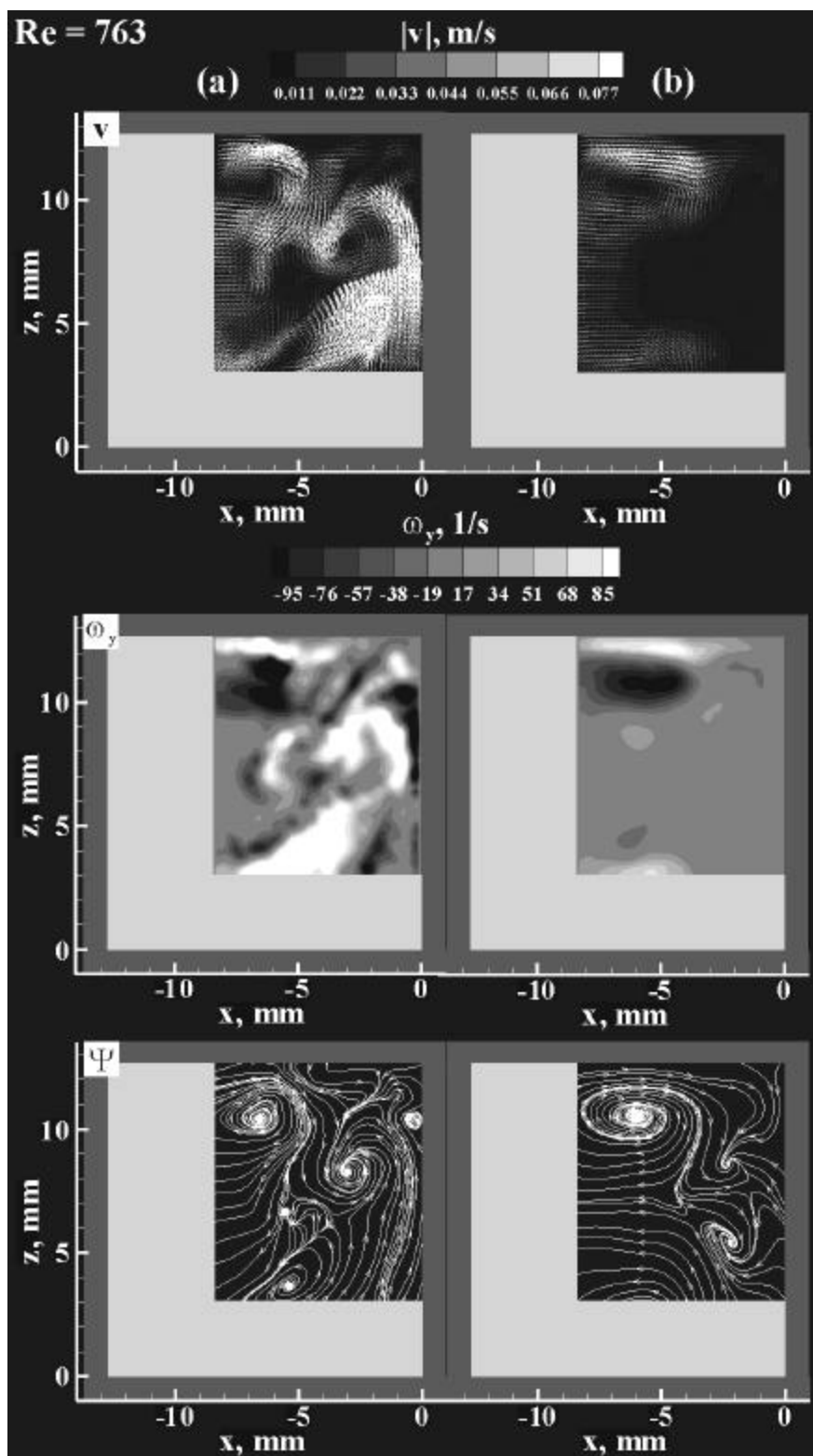
Figure B.5: (a) Instantaneous and (b) averaged flow fields for the secondary flow plane at Re = 763. From top to bottom: velocity vector field; out-of-plane vorticity contours; velocity streamlines.